https://doi.org/10.5194/egusphere-2025-5877
Preprint. Discussion started: 19 January 2026

High-resolution inversion of methane emissions over Europe using the Community Inversion Framework and FLEXPART

Anteneh Getachew Mengistu[1], Aki Tsuruta[1], Antoine Berchet[2], Rona Thompson[3], Maria Tenkanen[1], Hannakaisa Lindqvist[1], Tiina Markkanen[1], Antti Leppänen[1], Antti Laitinen[1], Adrien Martinez[2], Audrey Fortems-Cheiney[4], Lena Höglund-Isaksson[5], and Tuula Aalto[1]

[1]Finnish Meteorological Institute, P.O. Box 503, 00101 Helsinki, Finland
[2]Laboratoire des Sciences du Climat et de l'Environnement, 91190 Gif-sur-Yvette, France
[3]Norsk Institutt for Luftforskning (NILU), Kjeller, Norway
[4]Science Partners, Quai de Jemmapes, 75010 Paris, France
[5]Air Quality and Greenhouse Gases Program (AIR), International Institute for Applied Systems Analysis (IIASA), 2361 Laxenburg, Austria

Correspondence: Anteneh Getachew Mengistu (anteneh.mengistu@fmi.fi)

Abstract. Constraining methane (CH_4) emissions at high spatial and temporal resolution is critical for accurate European greenhouse gas budgets and mitigation policy. We use the Community Inversion Framework to estimate monthly CH_4 fluxes across Europe 2017–2022 at 0.2° × 0.2°, coupling the FLEXPART and assimilating observations from 46 in situ stations, including ICOS and non-ICOS sites. Prior emissions combine GAINS and EDGARv8 anthropogenic inventories with GFED biomass burning, JSBACH-HIMMELI wetland fluxes, and climatological natural sources. The inversion markedly improves agreement with atmospheric observations (r^2 = 0.87, RMSE = 24.35 ppb, mean bias = –2.14 ppb), performing best at northern European stations. Posterior EU27+3 CH_4 totals 23.28 ± 0.36 Tg CH_4 yr^{-1}, 6.6 % above the prior. Anthropogenic emissions average 17.6 ± 0.3 Tg CH_4 yr^{-1}, exceeding GAINS by 11 %, EDGARv8 by 4 %, and UNFCCC NGHGI (2023) by 3 %, consistent with recent studies. Country-level differences are substantial: emissions are higher in BENELUX (+54 %), Germany (+37 %), and France (+10 %), and lower in the UK (-11 %), Romania (-25 %), Poland (-16 %), and Italy (-11 %) compared to UNFCCC NGHGI (2023). Sectoral changes primarily reflect agricultural increases in western and central Europe, with reductions in northern wetlands and southern geological sources. Sensitivity tests highlight the influence of horizontal correlation length and the value of dense observational networks for refining regional CH_4 budgets.

1 Introduction

Methane (CH_4) mole fractions in Earth's atmosphere have nearly tripled since 1750, significantly contributing to a 0.6°C rise in global temperatures since the pre-industrial era (Saunois et al., 2020; Chen et al., 2022; Shen et al., 2023). The World Meteorological Organization (WMO) has reported record increases in global methane levels from 2020 to 2021, with further rises observed in 2022 (WMO, 2023). These increases pose substantial challenges, such as accelerating climate change, disrupting ecosystems, and complicating efforts to meet international climate goals. In response to these challenges and the urgent need to mitigate climate change, countries have pledged to reduce methane emissions by 30 % from

https://doi.org/10.5194/egusphere-2025-5877
Preprint. Discussion started: 19 January 2026

2020 levels by 2030, aiming for a 0.2°C reduction in global temperatures by 2050 (Cael and Goodwin, 2023). Similarly, the European Commission aims to achieve a climate-neutral Europe by 2050, as outlined in the European Climate Law (https://eur-lex.europa.eu/legal-content/EN/TXT/?uri=celex%3A32021R1119, last access: 30 October 2025), which mandates net-zero greenhouse gas (GHG) emissions (Rayner and Jordan, 2016). To effectively meet this goal, strategies must address reductions in both methane and carbon dioxide emissions, as both are crucial for mitigating global temperature rise. Methane is a significantly more potent greenhouse gas than carbon dioxide, with a global warming potential 28 times greater over a 100-year period and 84 times greater over 20 years (IPCC, 2023; Myhre et al., 2013; Saunois et al., 2020). As a result, reducing methane emissions offers an especially effective short-term strategy for mitigating overall greenhouse gas emissions (Dlugokencky et al., 2011; Kikstra et al., 2022). Achieving this, however, requires accurate estimates of methane emissions. Despite substantial research, considerable uncertainty remains in identifying the geographic and temporal sources of these emissions. Current national methane estimates reported to the UNFCCC predominantly rely on bottom-up methodologies, which apply emission factors to activity data, often supplemented by facility-specific information. However, these inventories are affected by significant uncertainties, often varying by a factor of two or more (Saunois et al., 2020; Solazzo et al., 2021), primarily due to the considerable variability in emission intensity across sources such as landfills, gas production facilities, and distribution networks (Leip et al., 2018). This variability cannot be fully captured by the use of generic emission factors, leading to substantial uncertainty in the resulting estimates. The reliance on uncertain and sparse input data, combined with poorly characterized emission factors, further undermines the accuracy of these estimates, especially when lacking comprehensive characterization. Moreover, since NGHGIs by design include only anthropogenic emissions, they do not account for natural methane sources and sinks. Therefore, complementary top-down approaches are essential to provide a more complete understanding of the total methane budget and to better constrain both anthropogenic and natural components.

To address these challenges, top-down approaches have increasingly been employed to generate independent, optimized emissions estimates. These methods use inverse techniques that assimilate observational data from in situ and/or satellite observations. Such estimates help to refine and constrain the data from bottom-up inventories. In recent years, the growing availability of greenhouse gas measurements and advancements in regional monitoring networks, particularly in Europe and North America, have significantly bolstered the effectiveness of top-down approaches (Bergamaschi et al., 2015). Numerous atmospheric inverse modelling studies have demonstrated the effectiveness of these approaches in quantifying methane emissions across regional to national scales. Such analyses have provided essential constraints on source magnitudes and spatial distributions, thereby informing climate mitigation strategies and policy development (e.g., Bocquet and Sakov, 2013; Saunois et al., 2020, 2025; Qu et al., 2021; Bergamaschi et al., 2022; Chen et al., 2022; Petrescu et al., 2021; Ernst et al., 2024; Petrescu et al., 2023; Steiner et al., 2024; Ioannidis et al., 2025). Complementing these scientific efforts, international initiatives such as the Global Carbon Project (GCP) (Friedlingstein et al., 2022), VERIFY (Petrescu et al., 2021), and EYE-CLIMA (https://eyeclima.eu, last access: 30 October 2025) have played a central role in developing coordinated frameworks for independent, observation-based assessments of greenhouse gas emissions and sinks. These programs integrate atmospheric observations, bottom-up inventories, and Earth system modelling to enhance transparency, support policy evaluation, and improve the robustness of emission estimates at regional to global scales. VERIFY, in particular, aimed to develop scientifically robust

https://doi.org/10.5194/egusphere-2025-5877
Preprint. Discussion started: 19 January 2026

tools for verifying national emission inventories by integrating atmospheric observations, satellite data, emission inventories, and ecosystem models. Building on these efforts, the EYE-CLIMA project has taken a step further by focusing explicitly on reducing uncertainties in inversion-based estimates of methane and other greenhouse gases. Similarly, GCP provides comprehensive global assessments of carbon sources and sinks, supporting transparency and consistency in reporting and informing international climate agreements. These coordinated efforts have laid the groundwork for standardized, policy-relevant verification systems that bridge the gap between scientific research and national reporting. These studies highlight the essential role of top-down approaches in enhancing the reliability of national methane inventories through independent verification. For example, Chen et al. (2022) identified a 21 % upward correction needed for the Chinese methane inventory reported to the UNFCCC in 2019, demonstrating how top-down methods can uncover significant underestimations in bottom-up data. Similarly, Bergamaschi et al. (2022) reported elevated methane emissions for Germany, France, and the BENELUX countries in 2018 compared to those reported to the UNFCCC, further showcasing the ability of top-down approaches to reveal higher emissions than those recorded by bottom-up inventories. In contrast, Bergamaschi et al. (2022) also showed a close alignment between top-down estimates and both anthropogenic and natural bottom-up inventories for the UK and Ireland, illustrating how these methods can also validate bottom-up data. Although atmospheric inverse modeling is widely recognized as a valuable tool for verifying bottom-up estimates (IPCC, 2006), its incorporation into national reports faces several challenges. These include the limited availability of high-quality atmospheric measurements and uncertainties in transport models. Additionally, most past top-down studies have focused either on total emissions or on specific regions, often lacking the spatial resolution and source attribution needed to provide robust estimates at the national or sectoral level. As a result, while progress has been made in constraining total methane fluxes, there remains a clear research gap in applying inverse modeling to optimize emissions from individual sectors such as agriculture, waste, fossil fuels, wetlands, and geological sources. This gap limits our ability to disentangle source-specific contributions, thereby constraining the design of targeted and effective mitigation strategies. Furthermore, the complexity of atmospheric processes and the resource-intensive nature of inversion systems present additional barriers to integrating top-down estimates into national inventory frameworks.

In this study, we address these gaps by presenting high-resolution atmospheric inversion estimates for CH_4 emissions over Europe, covering the domain between 12° W, 37° E and 35° N, 73° N. Using the Community Inversion Framework (CIF; Berchet et al. 2021), we apply a 4-dimensional variational optimization approach (4D-Var) driven by footprint estimates from FLEXPART v10.4 (Stohl et al., 1995; Pisso et al., 2019). The inversion assimilates data from 46 Integrated Carbon Observation System ICOS and non-ICOS in situ CH_4 observation sites across Europe (ICOS RI et al., 2023), providing monthly CH_4 emission estimates for the years 2017–2022 at a resolution of $0.2° \times 0.2°$. In addition to optimizing total methane emissions, our framework explicitly performs sector-specific optimization, enabling improved quantification of emissions from major sources including the energy sector, agriculture, waste management, wetlands, and geological sources. This dual approach strengthens both national-scale reporting and sectoral attribution, bridging a key gap in the current application of atmospheric inversions. Due to computational expenses of the calculations, sensitivity and uncertainty analyses were conducted using a representative sample month, serving also as a verification step to identify discrepancies in the optimized fluxes arising from inversion setup choices. By integrating both total and sector-resolved inversion estimates, our study provides a more detailed spatial and

https://doi.org/10.5194/egusphere-2025-5877
Preprint. Discussion started: 19 January 2026

source-specific characterization of methane emissions over Europe. These advances are crucial for informing climate policy, guiding sector-targeted mitigation strategies, and deepening scientific understanding of methane dynamics. The findings have the potential to substantially improve national reporting accuracy and support global efforts to reduce methane emissions in line with climate goals.

2 Datasets and Methodology

2.1 CIF-Flexpart Inversion Framework

We perform total and sector-specific methane inversions using the CIF coupled with a Lagrangian transport model FLEXPART and a 4D-Var optimization scheme, hereafter referred to as CIF-FLEXPART. CIF provides a unified platform for atmospheric inversions, supporting multiple transport models and enabling consistent assessments of greenhouse gas fluxes and their uncertainties. The posterior estimate is obtained by 4D-Var approach that seeks the optimal state vector $\mathbf{x}$ through minimizing the cost function:

$$J(\mathbf{x}) = \frac{1}{2}(\mathbf{x}-\mathbf{x}_b)^{\mathrm{T}}\mathbf{B}^{-1}(\mathbf{x}-\mathbf{x}_b) + \frac{1}{2}(\mathbf{y}_o-\mathbf{H}(\mathbf{x}))^{\mathrm{T}}\mathbf{R}^{-1}(\mathbf{y}_o-\mathbf{H}(\mathbf{x})), \tag{1}$$

where $\mathbf{x}$ is the control vector of surface fluxes, $\mathbf{x}_b$ the prior estimate with covariance $\mathbf{B}$, $\mathbf{y}_o$ the observed CH_4 mole fractions, and $\mathbf{R}$ the observation error covariance. Efficient minimization of the cost function necessitates the computation of its gradient with respect to the control vector. This gradient is evaluated using the adjoint operator $\mathbf{H}^\top$ of FLEXPART:

$$\nabla J(\mathbf{x}) = \mathbf{B}^{-1}(\mathbf{x}-\mathbf{x}_b) - \mathbf{H}^\top\mathbf{R}^{-1}(\mathbf{y}_o-\mathbf{H}(\mathbf{x})), \tag{2}$$

which propagates mismatches between observed and modeled mole fractions back into the flux space. The minimization is performed iteratively using the M1QN3 quasi-Newton algorithm (Gilbert and Lemaréchal, 2009), a limited-memory variant of the variable metric method, which updates the state vector with each iteration. The iterations continue until the norm of the gradient falls below a preset convergence threshold, which in this study is set to 0.01 % of its initial value or a maximum of 30 simulations.

Unlike analytical Bayesian solutions, which explicitly compute the posterior covariance, the variational approach efficiently yields the maximum a posteriori flux estimate in high-dimensional settings. The analytical solution

$$\mathbf{x}_a = \mathbf{x}_b + \mathbf{K}\big(\mathbf{y}_o - \mathbf{H}(\mathbf{x}_b)\big),\ \mathbf{K} \quad = \mathbf{B}\mathbf{H}^\top\big(\mathbf{H}\mathbf{B}\mathbf{H}^\top + \mathbf{R}\big)^{-1},\ \mathbf{A} = \big(\mathbf{B}^{-1} + \mathbf{H}^\top\mathbf{R}^{-1}\mathbf{H}\big)^{-1}. \tag{3}$$

represents the exact solution, where $\mathbf{x}_a$ is the posterior (optimized) flux state, $\mathbf{K}$ is the Kalman gain matrix, and $\mathbf{A}$ is the posterior error covariance matrix. In high-resolution applications, iterative numerical methods such as M1QN3 provide a computationally tractable approximation, though the resulting posterior is not identical to the analytical solution. Accordingly, we adopt a variational 4D-Var framework with iterative minimization to optimize surface fluxes. The prior covariance matrix $\mathbf{B}$ is modeled as:

$$\mathbf{B} = \mathbf{D}^T \cdot \mathbf{C} \cdot \mathbf{D} \tag{4}$$

https://doi.org/10.5194/egusphere-2025-5877
Preprint. Discussion started: 19 January 2026

where $\mathbf{D}$ is a diagonal matrix representing relative flux uncertainties, set to 50 % of the prior fluxes for all optimized categories. The state vector is defined in physical flux units, with each element corresponding directly to the flux of a given category or grid cell. Accordingly, the variances in $\mathbf{D}$ are expressed relative to the prior flux magnitudes, representing proportional uncertainties in the physical flux values rather than dimensionless scaling factors. The matrix $\mathbf{C}$ contains the correlation structure, with off-diagonal elements modeled using a Gaussian function that decays exponentially with spatial distance r as $\exp(-r^2/l^2)$ (Gaspari and Cohn, 1999; Peters et al., 2005). The spatial correlation length is set to $l_{\text{land}} = 200$ km over land and $l_{\text{ocean}} = 500$ km over oceans, while the temporal correlation length is prescribed as 90 days.

Observational errors are represented by $\mathbf{R}$, which accounts for instrument precision, model representativeness, and transport model errors. A minimum uncertainty of 5 ppb is imposed on all station observations to account for ∼3 ppb of transport model error. To avoid biasing surface fluxes, joint optimization of surface emissions and background mole fractions is performed. Background uncertainties of 0.5 % (∼10 ppb) were applied, consistent with previous studies that used values in the range of 0.05–1 % (Thompson and Stohl, 2014; Szénási et al., 2021; Steiner et al., 2024; Ioannidis et al., 2025). We also tested a lower value of 0.05 % in sensitivity experiments.

In our setup, we optimize the initial mole fractions together with the fluxes, and the extended control vector is:

$$\mathbf{x} = \begin{bmatrix} \mathbf{f} \\ \mathbf{c}_0 \end{bmatrix}, \tag{5}$$

where $\mathbf{f}$ represents the fluxes to be optimized, and $\mathbf{c}_0$ represents the initial mole fraction. Optimizing $\mathbf{c}_0$ ensures the transport model starts from a consistent atmospheric state, which is crucial for species like CH_4 where early-time conditions affect the entire simulation. The correlation structure of $\mathbf{c}_0$ is defined consistently with the fluxes, using a Gaussian function that decays with spatial distance r as $\exp(-r^2/l^2)$ (Gaspari and Cohn, 1999; Peters et al., 2005). The spatial correlation length is set to $l_{\text{land}} = 200$ km over land and $l_{\text{ocean}} = 500$ km over oceans, while the temporal correlation length is prescribed as 30 days. This formulation allows CIF to adjust both the emissions and the initial atmospheric state to best match the observed mole fractions, while respecting the prior uncertainties and correlation structures.

For the sector-specific inversion, the control vector $\mathbf{x}$ is partitioned into distinct methane source sectors as:

$$\mathbf{x} = \begin{bmatrix} \mathbf{x}_{\text{Wetlands}} \\ \mathbf{x}_{\text{Agriculture}} \\ \mathbf{x}_{\text{Energy}} \\ \mathbf{x}_{\text{Waste}} \\ \mathbf{x}_{\text{Industrial}} \\ \mathbf{x}_{\text{Fire}} \\ \mathbf{x}_{\text{Geological}} \\ \mathbf{x}_{\text{Termites}} \\ \mathbf{x}_{\text{Ocean}} \end{bmatrix}, \qquad \mathbf{x} = \sum_i \mathbf{x}_i \tag{6}$$

https://doi.org/10.5194/egusphere-2025-5877
Preprint. Discussion started: 19 January 2026

where sub-vector $\mathbf{x}_i$ corresponds to emissions from sector i. The prior covariance $\mathbf{B}$ encodes both uncertainties and cross-sector correlations, thereby guiding how total flux adjustments are redistributed among sectors. By preserving the correlation structure in $\mathbf{B}$, the inversion allows sector-specific adjustments to be inferred from total flux constraints. Although this approach does not replace source-specific tracers (e.g., isotopes or co-emitted species), it provides a first-order quantification of sectoral contributions to methane variability.

2.2 FLEXPART in the Inversion Framework

We employ the Lagrangian Particle Dispersion Model FLEXPART v10.4 (Pisso et al., 2019), a widely used open-source transport model for simulating the dispersion and turbulent mixing of atmospheric tracers (Stohl et al., 1995). Within our inversion framework, FLEXPART is used to quantify source–receptor relationships (SRRs) between surface methane fluxes and atmospheric observations.

Meteorological input fields were taken from the ERA5 reanalysis of the European Centre for Medium-Range Weather Forecasts (ECMWF). We use hourly data on 137 vertical levels, regridded to a horizontal resolution of $1^\circ \times 1^\circ$. These data are pre-processed for FLEXPART using the FlexExtract toolbox (Tipka et al., 2020). FLEXPART is operated in backward mode: for each observation, 10,000 pseudo-particles are released at the receptor location and traced backward in time for 10 days. The resulting surface flux footprints are archived at an hourly temporal resolution with a spatial resolution of $0.2^\circ \times 0.2^\circ$ for the nested domain and $2^\circ \times 2^\circ$ for the global domain. The dominant atmospheric sink of CH_4 through oxidation by OH is explicitly represented in FLEXPART using the CH_4 + OH reaction parameters together with 3-D OH fields from GEOS-Chem. The particle residence time within each grid cell is proportional to the observation's sensitivity to fluxes in that grid cell, yielding the source–receptor sensitivity matrix

$$S_{ij} = \frac{\partial y_i}{\partial q_j}, \tag{7}$$

where S_{ij} represents the sensitivity of observation y_i to a surface flux q_j in grid cell j. These SRRs explicitly account for advection, turbulence, convection, and deposition processes (Stohl et al., 1995; Seibert and Frank, 2004; Pisso et al., 2019). For long-lived greenhouse gases such as CH_4, it is essential to represent not only local and regional flux contributions but also the large-scale background concentration (Thompson and Stohl, 2014). CIF accounts for this by employing two types of sensitivities within the observation operator: (i) surface-flux sensitivities, separated into nested-domain and outside-nested contributions, and (ii) three-dimensional (3-D) concentration sensitivities that are multiplied by external 3-D mole-fraction fields to represent the large-scale background. The modeled methane mixing ratio at receptor i is then given by

$$y_i^m = \sum_j S_{ij}^{\text{nest}}\, x_j^{\text{nest}} + \sum_j S_{ij}^{\text{out}}\, x_j^{\text{out}} + \sum_k S_{ik}^{\text{3D}}\, c_k, \tag{8}$$

where S_{ij}^{nest} and S_{ij}^{out} denote the FLEXPART sensitivities of observation i to surface fluxes inside and outside the nested domain, respectively, and S_{ik}^{3D} denotes the sensitivity to the CH_4 mole fraction in 3-D grid cell k. For the sector-specific inversion flux vectors x_j can be further decomposed into sectoral contributions x_{js} Eq. (6) (e.g., agriculture, wetlands, biomass

https://doi.org/10.5194/egusphere-2025-5877
Preprint. Discussion started: 19 January 2026

burning), such that the flux contribution y^{flux} becomes

$$y_i^{\text{flux}} = \sum_s \sum_j S_{ij}^{\text{nest}} x_{js}^{nest} + \sum_s \sum_j S_{ij}^{\text{out}} x_{js}^{out}. \tag{9}$$

Thus, each modeled observation combines (i) local and regional flux enhancements, optionally partitioned by sector, and (ii) large-scale background contributions from external 3-D mole-fraction fields.

2.3 In situ observations of CH_4 mixing ratio

We utilised surface concentration measurements primarily from the Integrated Carbon Observation System (ICOS), a comprehensive European dataset of atmospheric CH_4 concentration time series that serves as a crucial input for atmospheric inversion models. This dataset includes both quality controlled ICOS and non-ICOS observations. Our base inversion setup has assimilated data from 44 in situ measurements sourced from the obspack_CH_4_466_GVeu_v10.0_20240729 European CH_4 time series (ICOS RI et al., 2023). Additionally, we included data from two Finnish Meteorological Institute (FMI) stations, Kumpula and Sodankylä, which have been identified as reliable observation sites (Tsuruta et al., 2019; Tenkanen et al., 2025). To ensure robust observational constraints on CH_4 emissions, we applied the site selection criteria separately for each year, retaining only stations with at least 30 days of data coverage in each year. A preliminary screening was performed to exclude stations for which the model did not adequately reproduce observed variability or magnitude. This screening removed only one site, Ispra (IPR, Italy), which exhibited consistently low correlation and comparatively high bias relative to observations, consistent with previous studies (Steiner et al., 2024). In addition, stations TAC and ZSF were excluded because they fell within the same model grid boxes as WAO and HPB, respectively. Since the two stations in each grid box likely experience identical modelled conditions, the choice of which one to retain was arbitrary. Furthermore, several mountain stations in the Alps were removed due to the model's limited ability to represent complex topography at its resolution. For the sensitivity analysis, an additional set of 10 stations was included, comprising: (i) the station with poor model–observation agreement (IPR), (ii) stations located in grid boxes shared with another site, and (iii) the previously omitted Alpine mountain stations. These additional stations were included in the sensitivity analysis to assess the impact of observation network density. Figure 1a shows the locations of all observation sites and the nested modelling domain. The study domain spans 12° W, 37° E and 35° N, 73° N and is hereafter referred to as Domain/Europe. It is further subdivided into subregions: the 27 European Union member states (EU27) plus the United Kingdom, Norway, and Switzerland (EU27+3); and four subregional groupings (Northern, Central, Western, and Southern). A detailed list of countries within each subregion is provided in Appendix A Table A1. Figure 1b displays the daily-averaged concentration time series for each station, calculated over the assimilated hours only (see Appendix A Table A2 for a complete list of stations). For a detailed description of the measurement procedures and data processing, see (Ramonet et al., 2020; Hazan et al., 2016).

When multiple intake heights were available, such as at the Cabauw station, where intakes were positioned at 27, 67, 127, and 207 meters above ground level, we chose to use data exclusively from the highest intake height. This approach was adopted to mitigate the difficulties that transport models encounter in accurately representing concentration gradients close to the ground, where such gradients tend to be steep and variable. By selecting the highest intake height, we ensured that the

https://doi.org/10.5194/egusphere-2025-5877
Preprint. Discussion started: 19 January 2026

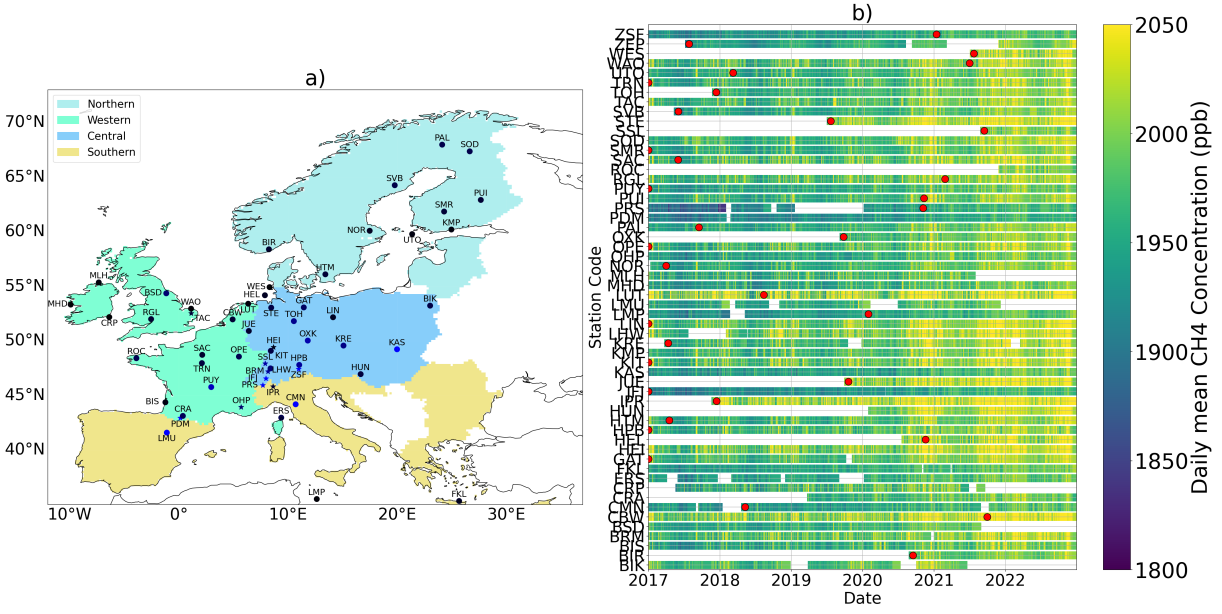

Figure 1. a) Distribution of the CH_4 observational network used in the inversion. Black dots: low-altitude stations (<1000 m a.s.l); blue dots: high-altitude stations (>1000 m a.s.l). Stations used in the sensitivity analysis are starred. EU27+3 countries are divided into four sub-regions, color-coded as in the legend. b) overview of daily mean CH_4 mole fractions from each assimilated station and ICOS levelling. Data after the red dot are ICOS-labeled. White gaps indicate periods with no data.

assimilated data effectively represented the characteristics of a well-mixed boundary layer, thereby improving the consistency of the methane modelled mole fraction (Vermeulen et al., 2011). Vertical gradients of CH_4 near the surface are notoriously difficult to simulate accurately due to factors such as complex local meteorology, surface interactions, and diurnal changes (Peltola et al., 2015). To mitigate these issues, we use recommended quality-controlled observations during periods when vertical gradients are expected to be lower, thus reducing potential errors in transport model simulations. For low-altitude sites ($\leq$ 1000 m a.s.l.) over relatively flat terrain, we assimilate 3-hour afternoon averages (14:00–16:00 LT), when the boundary layer tends to be well mixed and vertical mixing is strong. For high-altitude or mountainous sites (> 1000 m a.s.l.), we instead use 3-hour night-time averages (02:00–04:00 LT). These conditions are more likely to reflect free-tropospheric conditions and reduce contamination from daytime valley winds, which are challenging to represent at coarse model resolution. By focusing on these windows, we aim to mitigate biases associated with shallow, stable nocturnal layers and poorly resolved slope/valley circulations, thereby improving assimilation fidelity. This strategy is broadly consistent with practices in atmospheric inverse modeling, where daytime (often afternoon) observations are preferred for lowland sites to avoid difficulties in representing stable nocturnal boundary layers, and nighttime observations are often used in mountainous regions to limit the influence of unresolved diurnal circulations (Steiner et al., 2024; Monteiro et al., 2024).

https://doi.org/10.5194/egusphere-2025-5877
Preprint. Discussion started: 19 January 2026

2.4 Prior fluxes

High-resolution monthly data are employed for key contributors (anthropogenic, biospheric and fire) to capture fine-scale spatial variability and to identify localized hotspots. For sources with sparse data availability and limited temporal variability (ocean, geological and termites), coarser climatological estimates are used. However, all datasets are regridded to match the inversion spatial resolution (0.2°×0.2° for the nested European domain and 2°×2° for the global background). Within the nested European domain, agriculture is the dominant source, contributing approximately 11.7 Tg yr^{-1} (estimates for 2020, 34 % of the annual regional total). Other major contributors include waste (9.5 Tg yr^{-1}, 28 %), energy (5.5 Tg yr^{-1}, 16 %), geological emissions (5.1 Tg yr^{-1}, 15 %) and wetlands (2.9 Tg yr^{-1}, 9 %), smaller contributions arise from ocean (0.7 Tg yr^{-1}, 2 %), termites (0.6 Tg yr^{-1}, 2 %), industrial processes (0.03 Tg yr^{-1}, <1 %) and fires (0.03 Tg yr^{-1}, <1 %), with all estimates in brackets corresponding to the year 2020. These individual source contributions are then combined to calculate the total CH_4 prior emissions used in the inversion. A comprehensive overview of the prior data is provided in Table 1, with the corresponding map of mean fluxes for 2017–2022 shown in Appendix A Figure A1.

Table 1. Overview of CH_4 emission sources, their native resolutions, and average total emissions for the global and nested domains (Tg yr^{-1}). The reported values correspond to 2020 prior emissions.

Sector	Data Source	Native Resolution	Global	Nested Domain
Wetlands	JSBACH–HIMMELI for EU, LPX-Bern otherwise	0.10° × 0.10° daily	119.28	2.92
Agriculture	GAINS for EU27 + 3, EDGARv8 otherwise	0.10° × 0.10° monthly	134.10	11.74
Energy	GAINS for EU27 + 3, EDGARv8 otherwise	0.10° × 0.10° monthly	120.40	5.53
Waste	GAINS for EU27 + 3, EDGARv8 otherwise	0.10° × 0.10° monthly	87.85	9.52
Industrial Processes	EDGARv8	0.10° × 0.10° monthly	0.55	0.03
Fire	GFED4s1 (Van Der Werf et al., 2017)	0.25° × 0.25° monthly	11.42	0.03
Geological Sources	Etiope et al. (2019), global total scaled to 23 Tg	1° × 1° climatology	23.10	5.11
Termites	Saunois et al. (2020) climatology	1° × 1° climatology	9.91	0.56
Ocean	Weber et al. (2019)	1° × 1° climatology	9.35	0.71
Total			**513.96**	**36.15**

Monthly anthropogenic CH_4 emissions are derived from the Emission Database for greenhouse gas and Atmospheric Research (EDGARv8.0) (Crippa et al., 2020) and Greenhouse Gas and Air Pollution Interactions and Synergies (GAINS) (Höglund-Isaksson et al., 2020) inventories, both providing high-resolution (0.1° × 0.1°) global estimates of greenhouse gas emissions across multiple sectors. For EU27+3, we use emission estimates from the GAINS inventory, which incorporates country-specific activity data and mitigation assumptions, providing regionally consistent estimates that reflect national circumstances more closely than the globally uniform EDGARv8.0 inventory. On average, GAINS estimates are 3 Tg yr^{-1} (ranging from 1 to 4 Tg yr^{-1}) lower than EDGARv8.0, amounting to approximately 10 % of the total anthropogenic CH_4 emissions in the EU27+3 region during the study period. For categorising anthropogenic emission sources, we adopted the IPCC (2006)

https://doi.org/10.5194/egusphere-2025-5877
Preprint. Discussion started: 19 January 2026

Common Reporting Format (CRF) to classify the emissions into four main sectors: Energy, Industrial Processes and Product Use, Agriculture, and Waste. This sectoral breakdown is consistent with UNFCCC NGHGI reporting guidelines and used by major inventories such as GAINS and EDGAR, allowing for direct comparison with national reports.

Biospheric emissions in our prior estimates are sourced from the JSBACH model, which simulates key ecosystem processes such as photosynthesis, respiration, carbon and water cycling, vegetation dynamics, and land ecosystem processes (Reick et al., 2021). Specifically, we use the version of JSBACH coupled with HIMMELI (Raivonen et al., 2017) (JSBACH-HIMMELI), which provides hourly, high-resolution ($0.1^\circ \times 0.1^\circ$) CH_4 emissions, including contributions from peatlands, inundated soils and net mineral soils over Europe. As the JSBACH-HIMMELI product used in this study provides data only for the European domain, we complement it with global biospheric emissions from the LPX-Bern DYPTOP v1.4 dataset (Lienert and Joos, 2018) to represent the global background.

Monthly prior fire emissions are obtained from the Global Fire Emissions Database version 4 (GFED4s) described in van der Werf et al. (2017) at a spatial resolution of $0.25^\circ \times 0.25^\circ$, excluding methane emissions from biomass and agricultural waste burning, which were already included in GAINS and EDGAR. Oceanic CH_4 emissions are represented by climatological estimates from Weber et al. (2019), while geological emissions are based on the dataset by Etiope et al. (2019), globally scaled to 23 Tg yr^{-1}, following the Intergovernmental Panel on Climate Change (IPCC) AR6 Working Group I report (IPCC, 2023; Tsuruta et al., 2023). Termite-related emissions are included according to the estimates provided by Saunois et al. (2020).

2.5 Sensitivity Tests

We conducted eight inversion sensitivity experiments (S1–S8) to evaluate how key elements of the inversion setup influence the posterior CH_4 flux estimates and the associated error reduction. The base inversion (S1) serves as a reference for comparison. In S2, the background CH_4 mole fractions were replaced from CAMSv22r2 (Bergamaschi et al., 2013) to CTE-CH4 (Tenkanen et al., 2025) to evaluate the effect of background assumptions. Although both products rely on TM5-based transport (Krol et al., 2005), they differ in their inversion configurations, including data assimilation methods, flux resolution, prior constraints, and assimilated observations. Inversions S3 and S4 address uncertainty assumptions. In S3, the prior flux uncertainty was increased from 50 % to 100 %, allowing more flexibility for the inversion to adjust emissions. In S4, the uncertainty assigned to background mixing ratios was reduced from 0.5 % to 0.05 %, thereby increasing the influence of observed enhancements on the posterior flux adjustments. In S5, the observational network was expanded from 46 to 56 sites, including a denser station distribution along the Swiss Alps (see Fig. 1), to examine the sensitivity to observational coverage. In S6, the prior emissions were replaced from GAINS-based estimates to EDGARv8, which are approximately 10 % higher, allowing assessment of how differences in emission inventories affect the posterior flux estimates. Finally, S7 and S8 address spatial error correlations in the prior. The horizontal correlation length was reduced from 200 km to 50 km (S7) and 20 km (S8), enabling finer spatial adjustments in the inversion. All inversions were performed using a 4D-Var ensemble approach, where 30 Monte Carlo realizations were generated by perturbing both prior fluxes and observational data. Posterior uncertainties were estimated from the ensemble spread following Bocquet and Sakov (2013). The error reduction was computed as $1 - \frac{\sigma_{\text{post}}}{\sigma_{\text{prior}}}$, where σ_{post} and σ_{prior}

https://doi.org/10.5194/egusphere-2025-5877
Preprint. Discussion started: 19 January 2026

denote the posterior and prior uncertainties, respectively. Due to computational constraints, the sensitivity experiments were carried out for July 2021 only. A summary of the inversion configurations is provided in Table 2.

Table 2. Inversion setups for the sensitivity analysis. Deviations from the base inversion (S1) are indicated with an asterisk (*).

Sensitivity Case	**Initial Concentration**	**Prior Uncertainty**	**Initial Conc. Uncertainty**	**Number of Stations**	**Prior Dataset**	**Correlation Length**
S1	CAMSvr22	50 %	0.5 %	46	GAINS-based	200/500
S2	CTE-CH4*	50 %	0.5 %	46	GAINS-based	200/500
S3	CAMSvr22	100 %*	0.5 %	46	GAINS-based	200/500
S4	CAMSvr22	50 %	0.05 %*	46	GAINS-based	200/500
S5	CAMSvr22	50 %	0.5 %	56*	GAINS-based	200/500
S6	CAMSvr22	50 %	0.5 %	46	EDGARv8-based*	200/500
S7	CAMSvr22	50 %	0.5 %	46	GAINS-based	50/500*
S8	CAMSvr22	50 %	0.5 %	46	GAINS-based	20/50*

3 Results and discussion

3.1 Comparison of Simulated and Measured Methane Mole Fractions

Standard metrics such as mean bias, root-mean-square error (RMSE), and correlation play a crucial role in evaluating the performance of atmospheric inversion models by enabling direct comparison between simulated and observed CH_4 mole fractions. In this section, these metrics are applied to assess the CIF-FLEXPART inversion simulated mole fractions against the assimilated in situ observations. Figure 2 displays time series of both prior and posterior mole fractions from the base inversion set-up, alongside observations from selected European in situ stations in 2021, which cover a range of geographical settings and emission regimes. The prior methane mixing ratios generally underestimate the observations, resulting in a mean negative bias at most sites. In contrast, the posterior estimates substantially reduce this bias. These improvements are clearly visible in the time series Figure 2, which illustrate the discrepancies between observed and prior-simulated mole fractions and their correction in the posterior. For instance, at stations BIS, CRP, HPB, KIT, and TRN, the prior exhibits a pronounced negative bias (-11.11 to -22.39 ppb) and systematically underestimates sharp observational peaks when regional fluxes are elevated. The prior initial concentration contribution is overly smoothed and lacks the sharp variability of the observed and simulated mole fractions, though it still shows meaningful variations. The posterior reduces these biases (mean bias -3.21 to 3.82 ppb) and improves the representation of both the initial condition and regional flux contributions, providing a more realistic depiction of the regional signal. This adjustment is further reflected in the corresponding flux contributions in Appendix A Figure A2, where regional fluxes are increased in the posterior to better match the observations. At CBW, where local influences dominate, the prior fails to reproduce the full variability (see Fig. 2, CBW); the posterior reduces the overall bias, although some high-frequency discrepancies persist. The regional flux contributions show substantial adjustments in the posterior, consistent with

https://doi.org/10.5194/egusphere-2025-5877
Preprint. Discussion started: 19 January 2026

the improved match to observations. At PAL, prior mole fractions generally match observations, but pronounced mismatches occur during the first months of 2021. These were largely corrected by adjustments to the initial concentration contribution, while the global flux contribution remained relatively more influential and unchanged in the posterior (see Appendix A Figure A2). At ERS, unlike most other stations, the prior exhibits a mean positive bias of 8.53 ppb, which is reduced to 4.06 ppb in the posterior. The background contribution is adjusted upward, reinforcing the positive bias, while the regional flux contribution is lowered in the posterior. Together, these adjustments improve the overall agreement between simulated and observed mole fractions, illustrating the inversion's ability to correct both the initial condition and the regional flux components. Overall, these results demonstrate that the inversion effectively corrects biases in both the initial conditions and the regional fluxes, improving the representation of CH_4 dynamics across stations. These station-level mole fractions are further illustrated in Figure 3, which evaluates model–observation agreement across all stations and years (2017–2022). The coefficient of determination (R^2) increased from 0.54 to 0.76, RMSE decreased from 33.40 to 24.35 ppb, and mean bias was reduced from –12.20 to –2.14 ppb. The posterior regression slope (0.75) is closer to unity than the prior (0.57), and Pearson correlation increased from 0.78 to 0.87 ($p < 0.001$), reflecting enhanced responsiveness to observed changes. Modelled versus observation performance metrics for all assimilated stations are summarized in Appendix A Table A3. Our posterior statistical results closely align with the findings of (Steiner et al., 2024; Bergamaschi et al., 2022). By assimilating data from 28 stations, Steiner et al. (2024) reported a Pearson correlation of approximately 0.7 for 25 of the stations. Figure 3 also reveals that the prior simulation systematically underestimates high CH_4 mole fractions, with many data points falling below the regression line. This underestimation is particularly pronounced at stations such as LUT, LMU, STE, and CBW, all of which exhibit strong negative biases (below -35 ppb). Although the posterior simulation substantially reduces this underestimation, with biases improving to around -10 ppb, some discrepancies persist at the highest mole fractions, likely reflecting unresolved local emissions or sub-grid variability. These results highlight the importance of targeted improvements in emission inventories and model resolution for stations with persistent negative bias. To further assess the level of agreement across subregions, we compare posterior and prior simulations for different categories. This includes geographical regions (Central, Northern, Western, Southern) consistent with Petrescu et al. (2021), as well as elevation (mountain vs. non-mountain) and station type (coastal vs. non-coastal). Figure 4 presents the distributions of residuals using violin plots, with the 25th-75th interquartile range indicated by a vertical line. Posterior residuals exhibit systematically narrower spreads and improved alignment with observations. Across regions, RMSE and interquartile range (IQ75) decrease by 26–37 %, with median residuals moving closer to zero, except in the Southern region. Mountain stations show a smaller spread reduction (IQ75: 21.5 vs. 27.6, RMSE reduction 26 %), reflecting higher variability likely due to complex transport, whereas non-mountain, coastal, and non-coastal stations show 28–32 % RMSE reductions. Overall, these analyses demonstrate that the inversion effectively reduces uncertainty and bias across all categories, enhancing model fidelity and observational agreement (see Table 3).

https://doi.org/10.5194/egusphere-2025-5877
Preprint. Discussion started: 19 January 2026

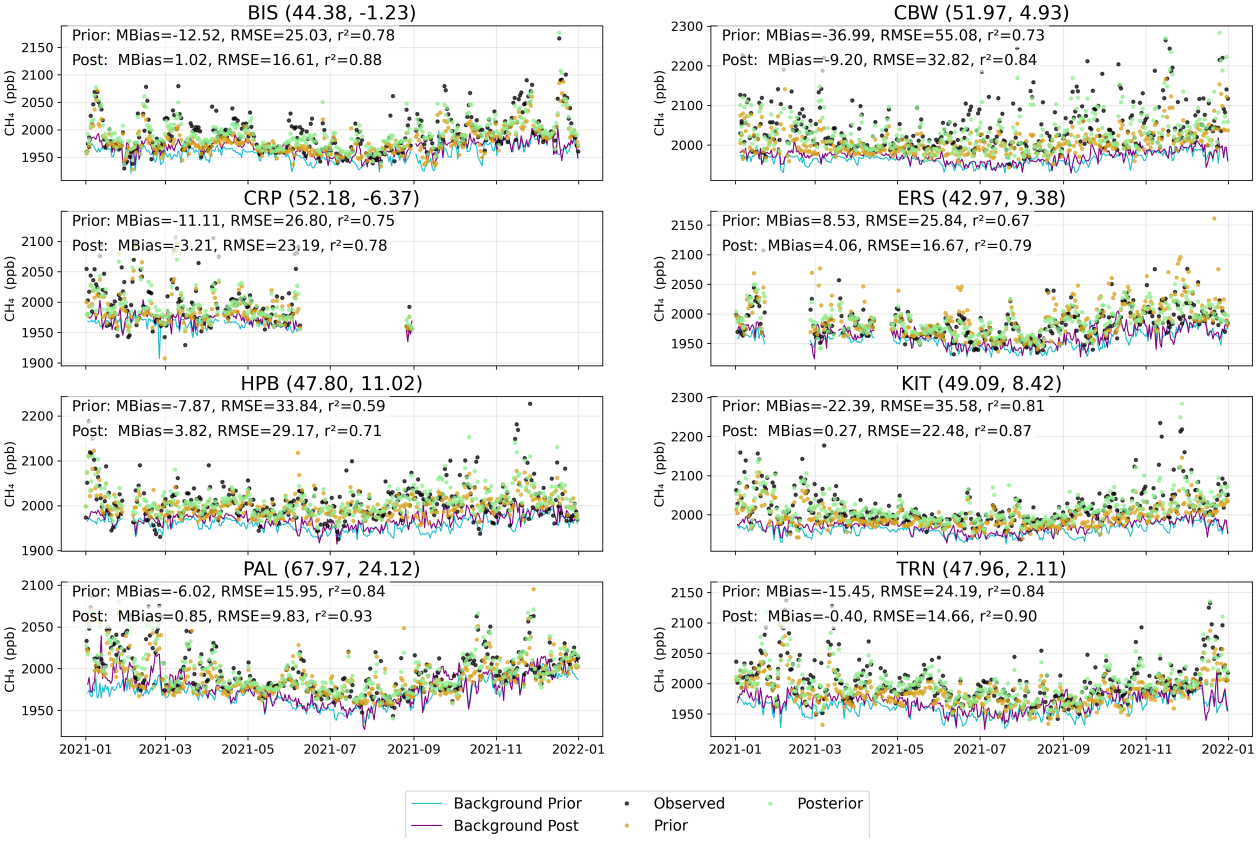

Figure 2. Time series of observed and modeled CH_4 mole fractions at selected stations, averaged at the assimilated hour for 2021: BIS (Biscarrosse, France), CBW (Cabauw, Netherlands), CRP (Carnsore Point, Ireland), ERS (Ersa, coastal Mediterranean site), HPB (Hohenpeissenberg, mountain station in Germany), KIT (Karlsruhe, Germany), PAL (Pallas, Finland), and TRN (Trainou, France), where the numbers in parentheses indicate the station's latitude and longitude. Shown are observations (black), prior simulations (orange), posterior simulations (green), and background contributions (cyan for prior, purple for posterior). Text boxes in each panel report mean bias (MBias), root mean square error (RMSE), and correlation coefficient (r^2) for the prior and posterior relative to the observations.

3.2 Posterior Flux

In Figure 5, we presented the six-year mean methane fluxes (2017–2022) over the study domain. Fig. 5(a–c) display prior estimates, posterior estimates, and their differences, while Fig. 5(d–e) present monthly time series and inland average estimates for subregions. The spatial maps highlight regions of substantial flux adjustments, and the time series illustrate temporal variability and regional contrasts between prior and posterior estimates. The inversion reveals pronounced regional corrections, with posterior emissions being systematically higher over BENELUX, France, and Germany, pointing to underestimation in the

https://doi.org/10.5194/egusphere-2025-5877
Preprint. Discussion started: 19 January 2026

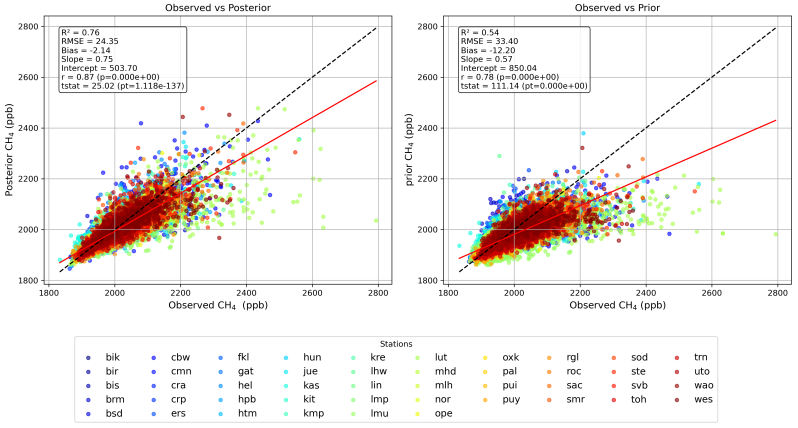

Figure 3. Modeled versus observed CH_4 mole fractions for all assimilated in situ observations. Left panels: posterior vs. observations; right panels: prior vs. observations. Statistical metrics are shown in each panel. Black dashed line: one-to-one; red line: best-fit regression.

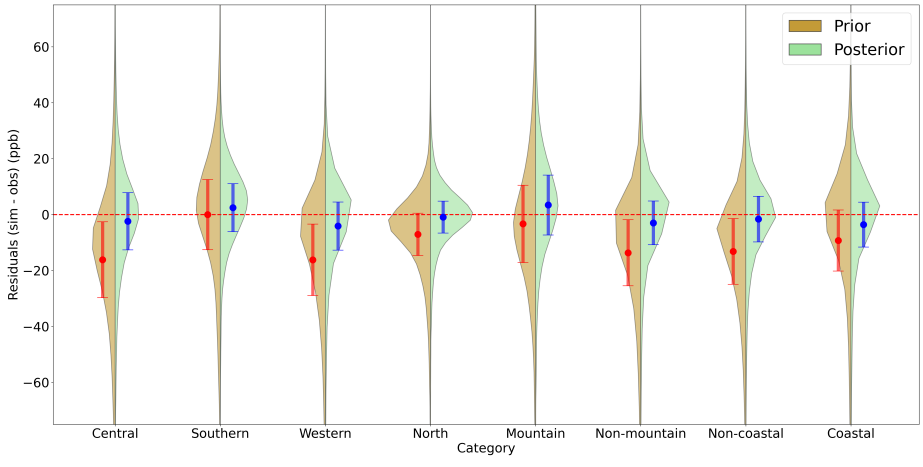

Figure 4. Residuals between observed (obs) and modelled (sim) CH_4 concentrations for assimilated in situ stations, grouped by subregional category (see Appendix A A2) The horizontal dashed line indicates zero residual, and the vertical bar shows the 25th–75th interquartile range. Negative values indicate that simulated concentrations are lower than observed.

prior, whereas reductions occur over the United Kingdom, Italy, and Romania, indicating prior overestimation. These patterns
335 align well with earlier inversion studies (Bergamaschi et al., 2022; Steiner et al., 2024). In regions with sparse observational data, such as the Iberian Peninsula and eastern Europe, the prior fluxes change only slightly.

Despite these pronounced regional adjustments, the mean emission exhibits only a modest net change at the domain scale, with average total methane emissions shifted 36.11 ± 0.38 Tg yr^{-1} in the prior to 36.72 ±0.62 Tg yr^{-1} in the posterior, a rise of 1.69 % (see Fig. 5d), reflecting strong subregional contrasts. Notable posterior CH_4 flux increases are observed in
340 Central Europe (+32 %) and Western Europe (+19 %), in contrast, Southern Europe shows a decrease of 17 % (see Fig. 5e).

https://doi.org/10.5194/egusphere-2025-5877
Preprint. Discussion started: 19 January 2026

Table 3. Prior and posterior performance metrics of CH_4 mole fraction simulations grouped by sub-regional category (see in Appendix A Table A2. Reported statistics include regional mean bias, the interquartile ranges: the 25th–75th (IQ75), and the 5th–95th range (IQ95), root mean square error (RMSE), relative RMSE reduction (ΔRMSE), number of observation stations, and the total number of data points (N-data) used in the evaluation.

Metric	Central		Southern		Western		North		Mountain		Non-mountain		Non-coastal		Coastal	
	Prior	Posterior	Prior	Posterior	Prior	Posterior	Prior	Posterior	Prior	Posterior	Prior	Posterior	Prior	Posterior	Prior	Posterior
Bias (ppb)	-16.14	-2.38	-0.0	2.5	-16.2	-4.1	-7.1	-0.9	-3.3	3.4	-13.6	-3.0	-13.1	-1.6	-9.3	-3.6
IQ75 (ppb)	27.17	20.44	25.1	17.1	25.6	17.2	15.1	11.4	27.6	21.5	23.6	15.7	23.5	16.3	21.8	16.1
IQ95 (ppb)	97.67	73.64	86.9	49.1	91.1	65.4	52.4	38.9	91.6	66.3	82.3	58.2	80.0	58.4	99.1	66.3
RMSE (ppb)	36.27	25.24	27.9	17.7	40.0	28.1	18.8	13.1	29.9	22.2	33.9	23.4	30.7	20.8	40.8	29.6
ΔRMSE (%)	30		37		30		30		26		31		32		28	
Stations	16		5		15		10		6		40		33		13	
N-data	24886		8354		27038		19897		11086		69089		60904		19271	

The monthly time series reveals a clear seasonality in northern regions, with a peak in summer months. The southern region exhibits a slight opposing seasonality, while other regions show no clear seasonal cycle. Additionally, it displays that posterior emissions from Central and Western Europe are consistently higher than the prior throughout the study period, while in the southern region, the posterior emissions are generally lower than the prior. At the domain and EU27+3 scales, however, there is no clear or persistent difference between posterior and prior emissions, and no significant trend is evident over the 2017–2022 period at either the domain or subregional scale. Over the EU27+3, the average posterior flux for 2017–2022 is 23.28 ± 0.36 Tg yr^{-1}, representing a 6.6 % increase relative to the prior. For EU27+UK, the posterior flux is 22.67 Tg yr^{-1}, which falls within the 22–26 Tg yr^{-1} range reported by Petrescu et al. (2021, 2023) for 2006–2017 based on three inversion setups. Although our estimate is at the lower end of this range, it provides a meaningful comparison given the difference in time periods, as EU27+UK emissions show no strong trend over the interval considered.

While spatial patterns in total methane flux adjustments indicate where the inversion has modified prior estimates, analysing these changes by sector reveals the dominant sources driving regional flux adjustments and highlights systematic biases in prior inventories. Figure 6 presents the spatial distribution of sector-specific methane flux increments (posterior – prior) over Europe for 2017–2022. Panels (a–d) correspond to anthropogenic sectors: agriculture (AGR), energy (ENG), waste (WST), and industry (IND); whereas panels (e–g) depict natural sources, including wetlands (WET), geological seepage (GEO), and biomass burning (FIR). Posterior agricultural emissions increase markedly across the BENELUX region, suggesting systematic underestimation in the prior inventory. Adjustments in other anthropogenic sectors are generally more spatially localized. Energy-related emissions decrease over the North Sea, but localized increases are observed in Belgium, Luxembourg, Ukraine, and western Russia. Waste emissions show localized hotspots in BENELUX, France, and Poland, while decreasing in Italy and the United Kingdom. Industrial emissions rise predominantly over BENELUX and Germany. CH_4 emissions from wetland are reduced, particularly in northern Europe and the United Kingdom, largely reflecting a reduction in summer fluxes. Reductions in the GEO sector over Italy and Romania are consistent with previously reported overestimations arising from globally scaled geological emission factors. Although prior geological emissions were harmonized to 23 Tg yr^{-1} at the global scale, the inver-

https://doi.org/10.5194/egusphere-2025-5877
Preprint. Discussion started: 19 January 2026

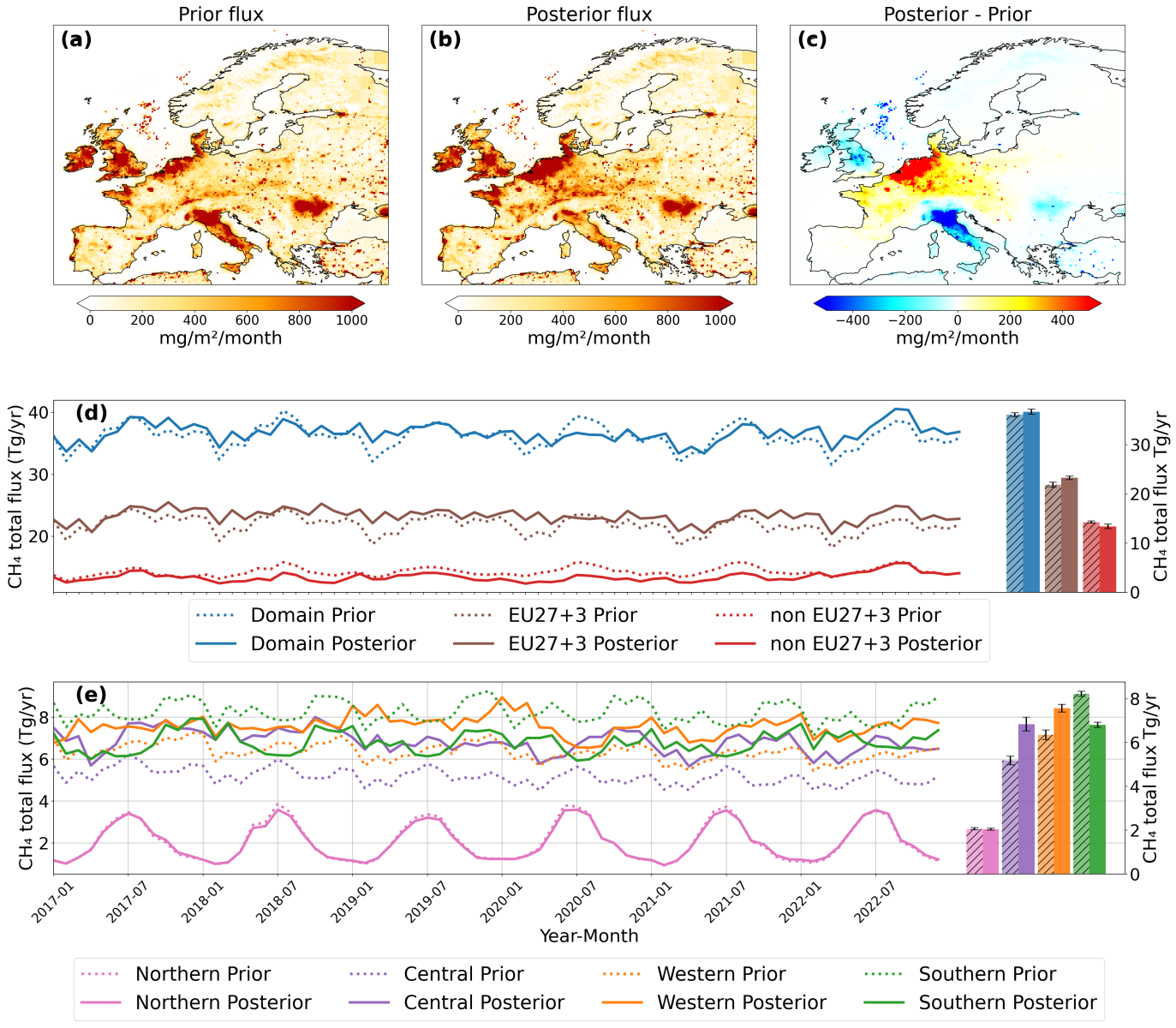

Figure 5. Top row: Mean methane (CH_4) fluxes over the EU27+3 domain for the study period (a) prior fluxes, (b) posterior fluxes after inversion, and (c) flux increments (posterior – prior). Middle rows: Monthly CH_4 flux time series averaged over the entire domain, within EU27+3, and outside EU27+3. Bottom row: Monthly CH_4 flux time series for selected EU27+3 subregions (Northern, Central, Southern, and Western), showing prior (dashed lines) and posterior (solid lines) estimates. Bars on the right summarize mean annual prior and posterior fluxes estimates (with a 1σ interannual variability).

sion results underscore the need for regionally differentiated adjustments. Biomass burning emissions increase over Portugal,
365 with minor reductions elsewhere.

https://doi.org/10.5194/egusphere-2025-5877
Preprint. Discussion started: 19 January 2026

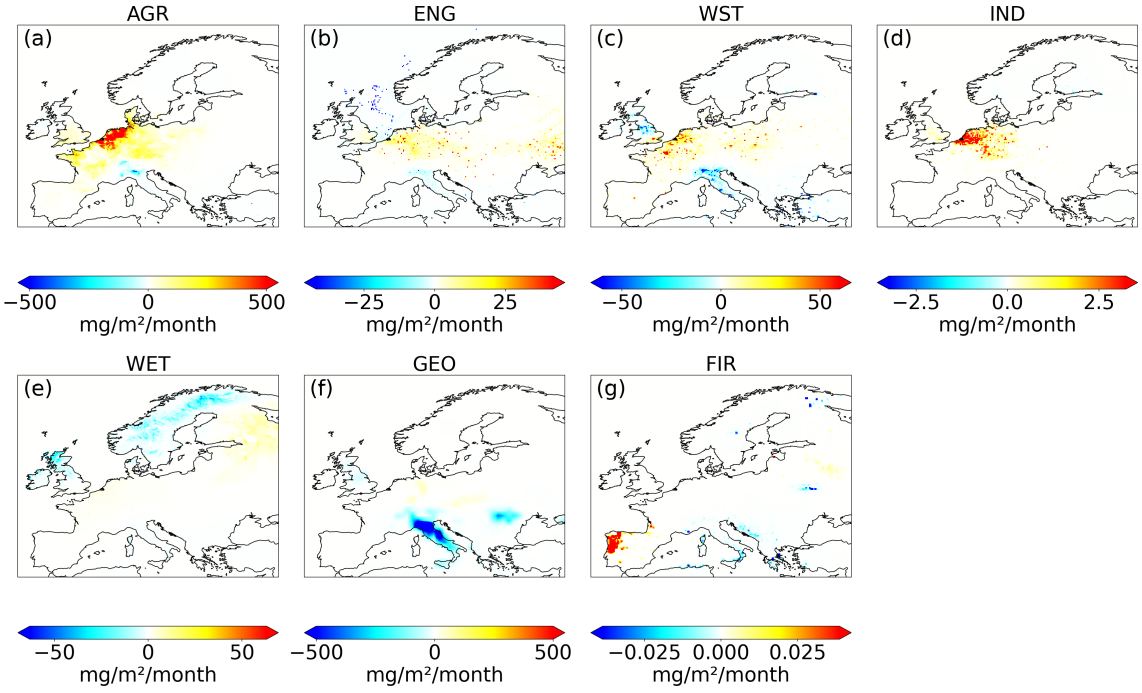

Figure 6. Spatial distribution of sector-specific methane flux increments (posterior - prior) over Europe averaged in the years (2017–2022). Panels show adjustments for agriculture (AGR), energy (ENG), waste (WST), industry (IND), wetlands (WET), geological sources (GEO) and fires (FIR). Agricultural emissions exhibit the largest posterior increase, particularly across central and western Europe, whereas wetlands show strong reductions in northern Europe. Geological emissions decrease mainly in southern Europe and Romania. Note that the colour scale is different.

Figure 7 summarizes the prior and posterior fluxes by European subregion. Agricultural emissions show the largest positive adjustments. In central EU27+3, emissions increase from a prior estimate of 2.37 to a posterior estimate of 3.19 Tg yr^{-1} (+35 %), and in western EU27+3 they rise from 3.51 (prior) to 4.54 Tg yr^{-1} (posterior), which is a 29 % rise. The strongest relative increase occurs in the BENELUX region, where mean agricultural emissions nearly double from 0.68 to 1.29 Tg yr^{-1} (+90 %).
370 At the domain scale, posterior agricultural CH_4 emissions amount to 13.63 Tg yr^{-1}, representing a 16 % increase compared with the prior. EU27+3 posterior emissions are estimated at 10.82 Tg yr^{-1}, corresponding to a 21 % increase relative to the GAINS prior (Fig. 7a). Agricultural emissions account for 46 % of the total EU27+3 CH_4 budget in our estimate, representing the largest sectoral share. This aligns with consolidated assessments and UNFCCC NGHGI reports, which attribute 52.4 % (±8.7 %) of EU27+UK CH_4 emissions in 2019 to agriculture (Petrescu et al., 2021, 2023). The dominant role of agriculture
375 in total anthropogenic CH_4 emissions also holds globally (IPCC, 2019). Emissions from energy-related sectors show modest increases in central Europe, rising from 0.81 to 0.87 Tg yr^{-1} (+8 %), and in western Europe, from 0.31 to 0.32 Tg yr^{-1} (+3 %).

https://doi.org/10.5194/egusphere-2025-5877
Preprint. Discussion started: 19 January 2026

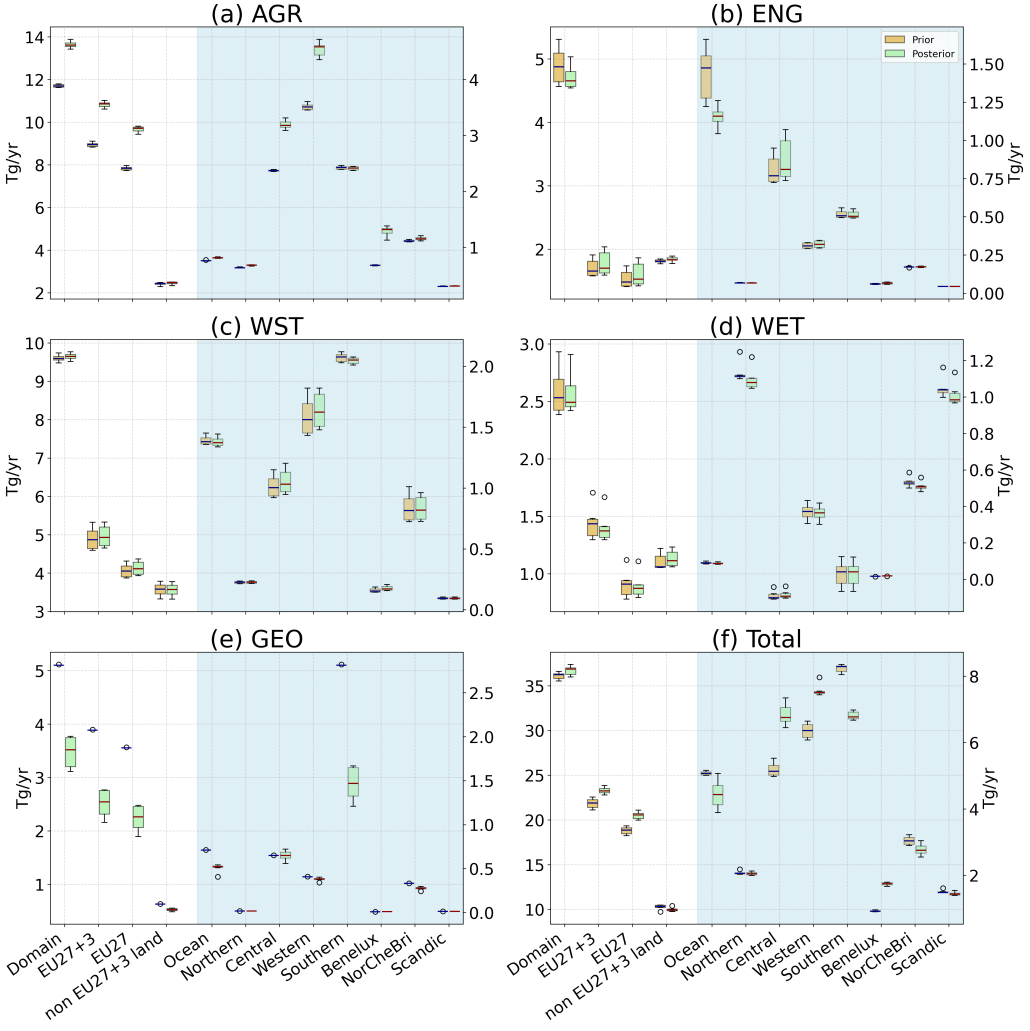

Figure 7. Mean estimates of prior and posterior CH_4 fluxes averaged over Europe and its subregions for the years 2017–2022. The panels display boxplots for total CH_4 emissions (Total), agriculture (AGR), energy (ENG), waste (WST), wetlands (WET), and geological sources (GEO). Boxplots within the yellow-shaded area of each subpanel (Ocean - Scandic) correspond to smaller regions and are plotted against the right-hand y-axis.

In contrast, emissions decrease over oceanic regions from 1.44 to 1.15 Tg yr^{-1} (–20 %), largely reflecting reduced fossil fuel contributions (Fig. 7b). Waste-sector emissions show relatively minor adjustments at the regional and subregional scales, reflecting compensating regional contrasts. Posterior corrections are nevertheless evident in specific hotspot regions (Fig. 7c), with increases in BENELUX, France, and Poland, and decreases in the United Kingdom and Italy, highlighting substantial country-level heterogeneity. Wetland emissions decrease slightly in northern Europe, from 1.13 Tg yr^{-1} (prior) to 1.10 Tg yr^{-1} (posterior) (–3 %), largely due to reductions during summer months, as well as in the UK, Ireland, Italy, and coastal areas,

https://doi.org/10.5194/egusphere-2025-5877
Preprint. Discussion started: 19 January 2026

indicating minor overestimations in these regions. In contrast, increases are observed in Eastern Europe and BENELUX (see Fig. 7d). CH_4 emissions from geological seepage decline sharply in southern Europe, from 2.8 Tg yr^{-1} in the prior estimate to 1.47 Tg yr^{-1} in the posterior, representing a 48 % reduction, primarily driven by substantial decreases in the previously overestimated emissions from Italy and Romania (Steiner et al., 2024) (see Fig. 7e). Details of regional and sectoral posterior fluxes estimates are provided in Appendix A Table A4. Total CH_4 emissions increase at the EU27+3 level, mainly in western and central Europe, while decreases occur in southern and oceanic regions (Fig. 7f). Overall, these posterior flux adjustments highlight that anthropogenic activity, especially emissions from agriculture and waste, drives most of the net increase in CH_4 emissions, while geological emissions decrease. These heterogeneous corrections underscore the importance of refining prior emission patterns at both sectoral and regional scales to develop robust methane budgets for Europe.

3.3 Temporal Variation of CH_4 Flux

Figure 8 illustrates the seasonal patterns of CH_4 emissions from the Agriculture, Energy, Waste, and Wetlands sectors, spatially aggregated across the EU27+3 subregions. Among these, the Wetlands sector in Northern Europe exhibits the most pronounced seasonality, with emissions peaking during the summer months, particularly in July. This pattern is primarily driven by warmer temperatures and consistently sufficient soil moisture, which together enhance microbial activity and methane production in wetland ecosystems (Bechtold et al., 2025; Aalto et al., 2025). The accelerated decomposition of organic matter under these conditions further contributes to elevated emissions during this period (Voigt et al., 2023). The red hatched shading in the figure indicates a posterior reduction in summer wetland emissions, suggesting a downward correction of potentially higher prior estimates in summer. The Waste sector shows notable seasonal patterns, particularly in Central EU27+3 countries, where emissions increase significantly during summer. This is likely due to intensified microbial decomposition of organic waste in warmer temperatures, leading to greater methane generation in landfills and wastewater treatment facilities. In contrast, the Southern EU27+3 countries display a distinct summer minimum in waste emissions, highlighting regional differences that may be influenced by climate or waste management practices. Emissions from the Energy sector exhibit an opposite seasonal trend, with a clear peak during the winter and a minimum in summer. This pattern is largely attributed to increased heating demand in colder months, resulting in higher fossil fuel combustion and methane emissions. Additionally, winter energy use often involves greater reliance on natural gas, which can lead to methane leakage from pipelines and storage systems, further contributing to wintertime emission peaks. These contrasting seasonal dynamics between sectors may counterbalance one another, contributing to the lack of a clear overall seasonal pattern in total CH_4 emissions at the regional scale. The Agriculture sector, by comparison, does not exhibit a distinct seasonal pattern across any of the regions. However, hatched blue shading in the figure indicates posterior increases in agricultural emissions over Central and Western EU27+3 countries, suggesting model adjustments based on observational constraints. These regional and sector-specific variations underscore the complexity of CH_4 emission dynamics and highlight the importance of disaggregated analyses to improve understanding and model representation of seasonal fluxes.

https://doi.org/10.5194/egusphere-2025-5877
Preprint. Discussion started: 19 January 2026

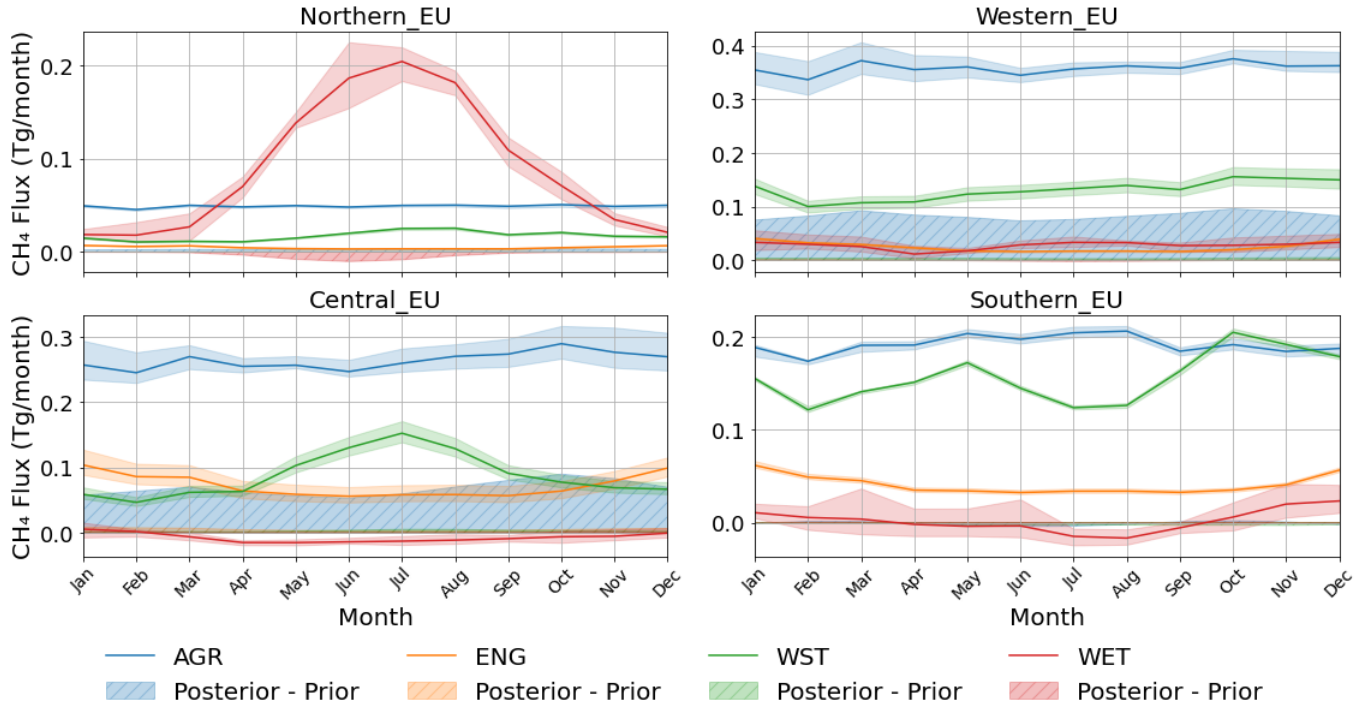

Figure 8. Seasonal patterns of CH_4 emission from major sectors, aggregated over the subregions for 2017–2022: (a) northern, (b) western, (c) central, and (d) southern Europe. The solid line represents the multi-year monthly mean, while the shaded area indicates the interannual variability (standard deviation). The hatched area shows the difference from the prior.

3.4 EU27+3 CH_4 Emission Estimates and Comparison with UNFCCC Reports

We calculated country-level anthropogenic CH_4 emission estimates for the EU27+3 and compared them with EDGARv8, GAINS, and UNFCCC NGHGI (2023) reports. Our posterior estimates averaged 17.6 Tg yr^{-1} for 2017–2021 (range: 17.0–18.2), with a mean annual decline of 0.3 Tg yr^{-1}. These posterior estimates are 11 % higher than GAINS, 4 % higher than EDGARv8, and 3 % higher than UNFCCC, indicating good overall consistency at the EU27+3 scale. They are also in close agreement with previous inversion studies; for example, Steiner et al. (2024) reported 17.4 Tg yr^{-1} for EU27+UK in 2018, compared to our estimate of 17.59 Tg yr^{-1} for the same region and year. The top three emitting countries (France, Germany, and the UK) accounted for 39 % of EU27+3 emissions, similar to inventories but with differing country rankings. The UK stood second in the UNFCCC report. However, larger discrepancies appear at the national level (see Fig. 9 and Appendix A Table A5). Compared with UNFCCC, posterior emissions are higher for BENELUX (+54 %), Germany (+37 %), and France (+10 %), but lower for Romania (–25 %), Poland (–16 %), and Italy (–11 %). Notable differences also occur in the Nordics, with decreases in Norway (–39 %), Finland (–16 %), and Denmark (–13 %), but an increase in Sweden (+10 %). Relative to EDGARv8, posterior estimates are higher for Portugal (+40 %), Italy (+18 %), and Germany (+10 %), but substantially lower in the UK

https://doi.org/10.5194/egusphere-2025-5877
Preprint. Discussion started: 19 January 2026

(–18 %), Poland (–7 %), Romania (–18 %), and especially the Nordics. Adjustments relative to GAINS are upward for Germany (+29 %), France (+16 %), and BENELUX (+40 %), but downward for Switzerland (–13 %) and Italy (–7 %). In addition to country-level discrepancies in total anthropogenic estimates, systematic patterns emerge across sectors, as displayed in Figure 9. In agriculture, inventories generally underestimate emissions in large agricultural countries such as France, Germany, and the Netherlands, whereas our posterior consistently suggests higher values. This implies that bottom-up activity data and emission factors may not fully capture agricultural methane sources. In the waste sector, EDGARv8 tends to overestimate emissions in countries like Germany and France but underestimates them in others, including the United Kingdom, Italy, and Poland. Our posterior estimates often fall closer to GAINS and UNFCCC values. For the energy sector, inconsistencies are more pronounced. In the United Kingdom, EDGARv8 clearly overestimates emissions, whereas in Poland and Romania, both EDGARv8 and UNFCCC report higher values than our posterior. These differences are likely driven by variations in fossil fuel activity data and the emission factors employed by different reporting frameworks. Overall, the EU27+3 total appears relatively robust across inventories, yet sectoral and country-level comparisons reveal significant discrepancies. Our inversion estimates provide an essential independent constraint in this context, helping to reconcile inconsistencies in bottom-up reporting systems and strengthening confidence in national and sectoral methane emission estimates.

3.5 Sensitivity Experiments and Their Impact on Optimised Flux Estimates

To assess the sensitivity of the inversion framework, we conducted eight inversions (S1-S8) by varying key parameters, including background mole fractions, prior flux and background mole fraction error assumptions, observational coverage, choice of prior inventories, and correlation assumptions detailed in Section 2.5. Figure 10 presents the resulting posterior flux increments and error reductions for July 2021. Inversion setups from S1 to S5 exhibit broadly consistent spatial patterns and magnitudes of posterior flux increments, though the degree of error reduction varies among cases. The base inversion setup (S1) achieves substantial reductions of 14 % for Europe and 21 % for EU27+3, with particularly strong constraints in Central Europe (38 %) and Western Europe (30 %) (see Table 4). S2 is nearly indistinguishable from S1 at both regional and subregional scales, showing only slightly weaker reductions in northern Europe, suggesting that posterior adjustments are relatively insensitive to the choice of background concentration. S3 and S4 yield somewhat weaker mean error reductions of about 16 % for EU27+3, indicating moderate sensitivity of posterior adjustments to prior uncertainty scaling and background error assumptions. Larger assumed background errors allow observations to exert a stronger influence, whereas smaller errors suppress corrections and increase reliance on the prior. Although these effects are modest in magnitude (–2 to +2 ppb), they highlight the critical role of background error settings in modulating inversion flexibility and posterior responsiveness. The influence of background error settings on concentration fields is illustrated in Fig. 11.

Network densification in S5 enhances error reduction across most regions, particularly in Western Europe, where reductions exceed 35 %. This improvement reflects the added influence of stations such as TAC in the United Kingdom and PDM and OHP in France, which help better constrain emissions over the UK and southern France. The additional mountain station in the Alps, however, does not show a clear enhancement in posterior uncertainty reduction, suggesting that its effectiveness may depend on representativeness or transport model resolution. Although the spatial pattern of posterior flux increments remains

https://doi.org/10.5194/egusphere-2025-5877
Preprint. Discussion started: 19 January 2026

Figure 9. Annual mean anthropogenic CH_4 emissions (2017–2021) for selected EU27+3 countries, shown as bar plots for the posterior estimates, GAINS, UNFCCC, and EDGARv8. Subpanels display CH_4 emissions from major anthropogenic sectors: (a) total anthropogenic emissions excluding land-use and land-cover change, (b) agriculture, (c) waste, and (d) energy. For each country and sector, bars are stacked by year, from bottom (2017) to top (2021).

consistent with earlier inversion setups, the expanded network clearly strengthens the overall robustness of the inversion. These

https://doi.org/10.5194/egusphere-2025-5877
Preprint. Discussion started: 19 January 2026

findings are consistent with previous studies demonstrating that increased observational density improves posterior reliability in well-sampled regions (Villani et al., 2010; Thompson and Stohl, 2014).

More pronounced differences emerge from the S6-S8 inversion setup. Using EDGARv8 as the prior (S6) increases the prior flux magnitude to 26.1 Tg yr^{-1} for EU27+3, compared to 24.5 Tg yr^{-1} in S1, reflecting EDGARv8's higher reported emissions. However, the posterior flux in S6 decreases substantially to 23.0 Tg yr^{-1}, closely aligning with the posterior estimate from the base inversion (S1). The 19 % mean error reduction in S6 is also comparable to S1, highlighting the sensitivity of inversion results to the choice of emission inventory and the convergence of posterior estimates despite differing priors. In contrast, reducing correlation lengths leads to diminished error reduction. At 50 km (S7), reductions are minimal (1–3 %), while at 20 km (S8) they are negligible (<0.2 %). This reflects the trade-off between allowing fine-scale flux variability and weakening the effective observational constraint per degree of freedom. Such behaviour is consistent with Thompson and Stohl (2014), who showed that extreme localization increases small-scale heterogeneity at the cost of inversion robustness.

Despite these sensitivities, the dominant spatial patterns of posterior corrections remain robust across sensitivity inversion setups: decreases over Italy, Romania, and the United Kingdom, and increases over BENELUX, Germany, and France. This consistency with previous European inversion studies (Saunois et al., 2020; Steiner et al., 2024) underscores the resilience of large-scale flux signals, even under varying methodological assumptions. Overall, S1 emerges as a balanced configuration, providing a reasonable compromise between observational constraint and inversion flexibility. Alternative setups highlight sensitivities to priors, background errors, and correlation lengths, but the preservation of large-scale spatial patterns across experiments supports the robustness of the main conclusions.

Figure 11 illustrates the background concentration changes and their sensitivity to background error assumptions. Under the larger background error scenario (0.5 % uncertainty), we found a systematic decrease in background CH_4 over the Northern and Mediterranean Seas, suggesting that the prior background fields were biased high in these regions (see Fig. 11b). The spatially averaged time series of the posterior increment exhibits a clear seasonal pattern, occurring from May to October (see Fig. 11d), reflecting the correction of this high bias through the inversion. Conversely, assuming a smaller error (0.05 %) resulted in much weaker corrections, both spatially (see Fig. 11c) and temporally (see Fig. 11d), as seen in the posterior mean increment time series. Under a low-error assumption, the inversion relies more strongly on the initial concentration estimates, limiting adjustments to the posterior background concentration field. Conversely, higher error assumptions allow the observations to exert greater influence, producing stronger corrections in regions where the prior background fields were biased.

Figure 11e shows the relative annual mean difference of the posterior fluxes under background error assumptions of 0.5 % and 0.05 %. The relative difference is defined as $1 - F_{0.5\%}/F_{0.05\%}$, where $F_{0.5\%}$ and $F_{0.05\%}$ denote the annual mean fluxes computed using background-error assumptions of 0.5 % and 0.05 %, respectively. Flux adjustments under these scenarios generally follow the spatial patterns of the mean map (see Fig. 5c), with additional corrections of approximately –20 % in regions showing decreases and +20 % in regions showing increases. An extreme reduction (–40 %) occurs over Italy, likely contributing to the observed posterior flux decrease. Overall, background-related adjustments remain modest (–2 to +2 ppb) and are secondary to the dominant sectoral flux corrections.

https://doi.org/10.5194/egusphere-2025-5877
Preprint. Discussion started: 19 January 2026

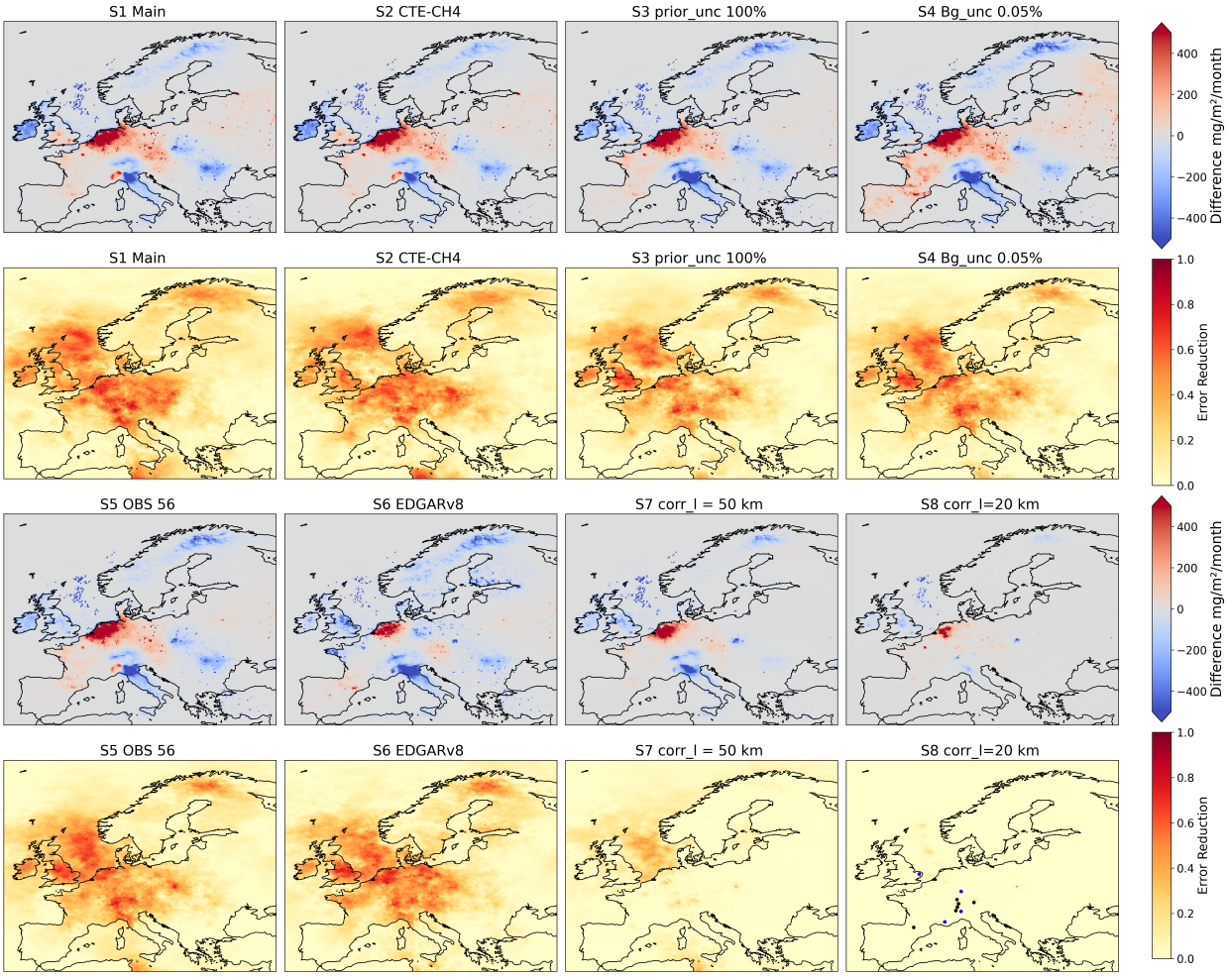

Figure 10. Flux increments (posterior - prior) and error reduction for July 2021 across eight sensitivity inversion setups (S1–S8). Each panel illustrates the spatial distribution of flux adjustments relative to the prior, highlighting the influence of varying prior emissions, background treatment, observational network density, and error correlation assumptions. The last subpanel displays the stations added for inversion setup S5. Mountain stations are shown as black dots, while low-altitude stations are shown as blue dots.

4 Conclusions

In this study, we have presented a high-resolution, top-down estimates of European CH_4 emissions for the period 2017–2022, offering robust new evidence on their magnitude, spatial structure, and temporal evolution across the continent. By combining the CIF-FLEXPART inversion framework with a 4D-Var data assimilation approach, we demonstrated the value of advanced atmospheric inverse modelling for resolving fine-scale emission patterns that are not accessible through conventional analytical inversion techniques. The use of FLEXPART-derived source–receptor sensitivities, together with the optimisation of a large set of control variables, enables a detailed representation of emission patterns at monthly timescales and a spatial resolution of 0.2°

https://doi.org/10.5194/egusphere-2025-5877
Preprint. Discussion started: 19 January 2026

Table 4. Prior, Posterior, and Mean Error Reduction (%) for different regions and sensitivity inversion setups (S1-S8) as described in Section 2.5

Prior (Tg yr^{-1})								
Region	S1	S2	S3	S4	S5	S6	S7	S8
Europe	38.65	38.61	38.30	38.37	38.37	40.33	38.51	38.53
EU27+3	24.51	24.59	24.30	24.36	24.36	26.07	24.48	24.49
Northern	4.01	4.04	3.97	3.98	3.98	4.61	3.99	3.99
Western	7.03	7.10	6.97	6.99	6.99	7.35	7.02	7.02
Central	5.93	5.92	5.85	5.87	5.87	6.31	5.92	5.92
Southern	8.08	8.07	8.04	8.06	8.06	8.36	8.09	8.09
Posterior (Tg yr^{-1})								
Region	S1	S2	S3	S4	S5	S6	S7	S8
Europe	37.06	37.20	35.43	36.92	36.52	36.02	36.34	38.09
EU27+3	24.10	24.40	23.01	24.08	23.80	22.99	23.70	24.42
Northern	3.63	3.70	3.43	3.39	3.56	3.55	3.75	3.96
Western	7.20	7.32	7.33	7.50	7.42	6.88	7.13	7.15
Central	6.79	6.79	6.33	6.79	6.33	6.29	5.97	5.86
Southern	7.19	7.30	6.60	7.11	7.19	6.90	7.52	8.05
Mean Error Reduction (%)								
Region	S1	S2	S3	S4	S5	S6	S7	S8
Europe	14.04	12.97	10.70	11.06	14.93	11.51	3.06	0.13
EU27+3	21.23	20.00	16.38	16.34	21.12	19.21	1.55	0.16
Northern	16.62	12.77	11.49	9.93	16.28	14.56	1.18	0.05
Western	29.96	30.38	27.53	28.53	35.76	28.82	3.37	0.39
Central	37.77	38.28	29.69	30.55	33.98	36.70	1.97	0.34
Southern	10.41	10.36	6.53	7.31	9.07	7.21	0.49	0.03

× 0.2°. The assimilation of observations from a dense network of 46 in situ monitoring stations substantially strengthens the observational constraints over Europe, leading to improved confidence in the inferred emissions and their sectoral attribution. By separately optimising emissions from major source categories, including agriculture, energy-related activities, waste management, industrial processes, wetlands, geological sources, and biomass burning, this work provides actionable information that is directly relevant to national inventories and mitigation strategies.

The posterior concentration in our study shows a great improvement with atmospheric observations (r^2 = 0.87, RMSE = 24.35 ppb, mean bias = –2.14 ppb) and captures most of the observed CH_4 variability. Our results reveal substantial regional-scale adjustments relative to prior inventories. Posterior emissions are consistently higher over the BENELUX region, France,

https://doi.org/10.5194/egusphere-2025-5877
Preprint. Discussion started: 19 January 2026

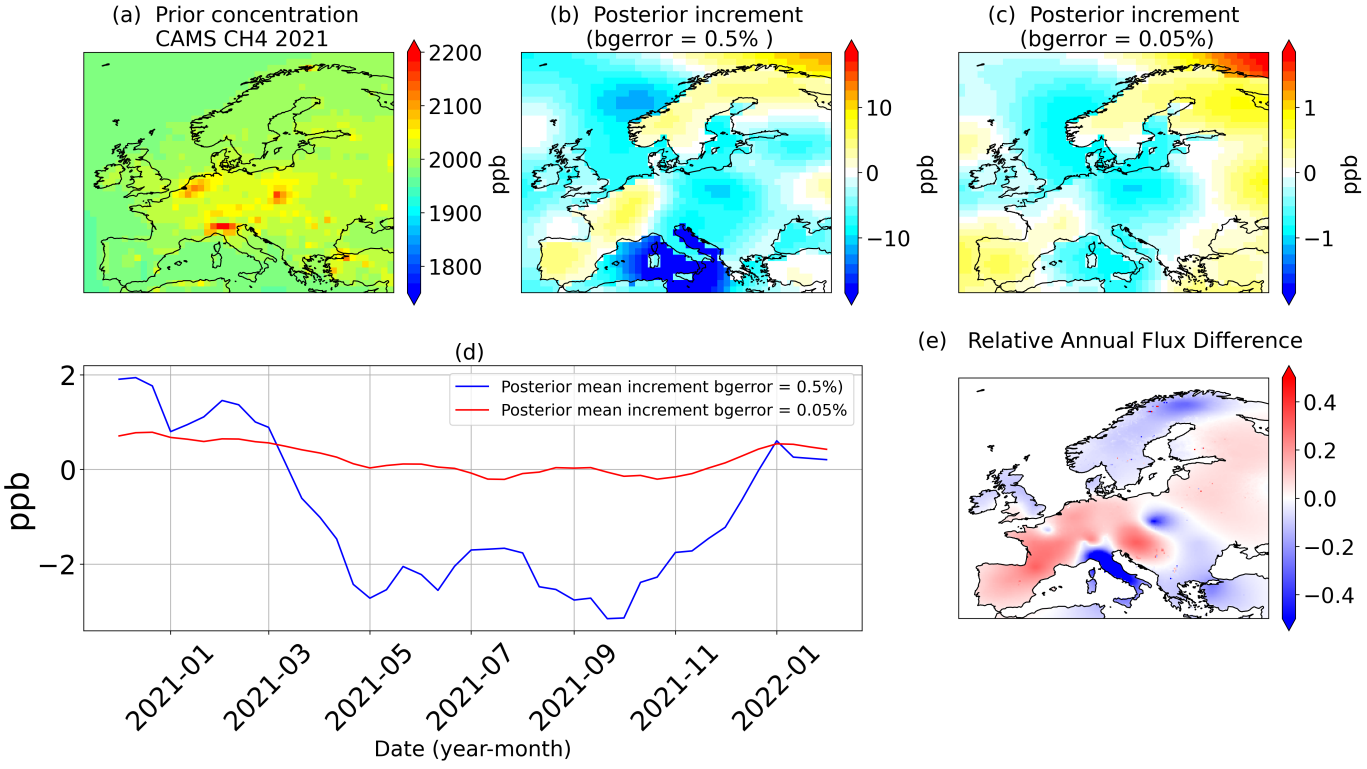

Figure 11. Impact of background error assumptions on optimized methane mole fractions and fluxes for 2021. Top row: (a) Prior mole fractions from CAMS and posterior increments with background error assumptions of (b) 0.5 % and (c) 0.05 %. Bottom row: (d) Time series of posterior mean increments under both settings and (e) relative annual flux difference between inversions with background errors of 0.5 % and 0.05 %. To quantify the impact of background-error assumptions, the relative difference was defined as $1 - \frac{F_{0.5\%}}{F_{0.05\%}}$, where $F_{0.5\%}$ and $F_{0.05\%}$ denote the flux computed using a background-error assumption of (0.5 %) and (0.05 %) respectively.

and Germany, suggesting underestimation in current inventories, whereas posterior reductions over the United Kingdom, Italy, and Romania indicate possible prior overestimation. These regional patterns are broadly consistent with earlier inversion studies (Bergamaschi et al., 2022; Saunois et al., 2020; Petrescu et al., 2021; Steiner et al., 2024), which lends confidence to their robustness. At the aggregated EU27+3 scale, our total posterior methane emissions are corrected from 21.84 ± 0.57 to 23.28 ± 0.36 Tg yr^{-1}, representing a modest 6.6 % rise compared with the prior. Although this is a modest overall increase, there are strong regional and sectoral differences. Anthropogenic CH_4 emissions are averaged 17.6 Tg yr^{-1} during 2017–2021 (range: 17.0–18.2 Tg yr^{-1}), corresponding to a mean annual decrease of 0.3 Tg yr^{-1}. These values are 11 % higher than GAINS, 4 % higher than EDGARv8, and 3 % higher than UNFCCC NGHGI (2023), indicating good overall consistency with bottom-up inventories and recent inversion-based estimates (e.g. Steiner et al. 2024). However, country-level comparisons reveal notable discrepancies: emissions are higher than reported for BENELUX (+54 %), Germany (+37 %), and France (+10 %), but lower for Romania (–25 %), Poland (–16 %), and Italy (–11 %). Notable decreases are also found for Norway (–39 %), Finland

https://doi.org/10.5194/egusphere-2025-5877
Preprint. Discussion started: 19 January 2026

(–16 %), and Denmark (–13 %), while Sweden exhibits a modest increase (+10 %), pointing to areas where inventory improvements are needed. Furthermore, our sectoral analysis indicated that agriculture is the dominant source of European methane emissions and the primary driver of the posterior increase, accounting for nearly half of total EU27+3 emissions and corrected upward by 21 % relative to the prior estimate. Energy-sector emissions show a small increase over land regions, while decreasing in coastal and ocean areas, and waste emissions remain broadly stable, despite pronounced national variability. In contrast, emissions from wetlands and geological sources show decreases, particularly reductions in wetland emissions observed during the summer months in Northern Europe and decreases in geological emissions in Italy, Romania, and the UK. In addition, we conducted eight sensitivity experiments by varying key parameters in the inversion setup. The results indicated that posterior fluxes show limited sensitivity to the choice of initial mole fractions and prior fluxes, underscoring the dominant role of atmospheric observations in constraining emissions. In contrast, assumptions regarding error correlation lengths and observational density strongly influence uncertainty reduction and the magnitude of posterior fluxes, emphasising the importance of realistic error characterisation and the continued expansion of atmospheric measurement networks.

Our study demonstrates that dense atmospheric monitoring combined with high-resolution inversion modelling provides a robust top-down framework to evaluate national inventories, identify regional emission hotspots, and support verification of methane mitigation efforts in Europe. By improving both spatial resolution and sectoral attribution, these results advance understanding of European methane sources and their variability, with direct relevance for climate policy and mitigation verification. Nevertheless, some limitations remain. Observational coverage is sparse in parts of eastern and southeastern Europe, limiting the ability to resolve emissions at finer spatial scales in these regions. Uncertainties in the transport model and assumptions about background CH_4 levels may also affect the posterior estimates. In addition, this study didn't systematically assess the impacts of different resolutions, grid-based uncertainty, different natural priors and OH fields. Thereby, future work should address these limitations through dedicated sensitivity analyses and by integrating satellite observations and isotopic signatures (e.g., $^{13}CH_4$) to improve source attribution, expand spatial coverage, and further strengthen European methane emission estimates.

Appendix A: Supplementary Figures and Tables

https://doi.org/10.5194/egusphere-2025-5877
Preprint. Discussion started: 19 January 2026

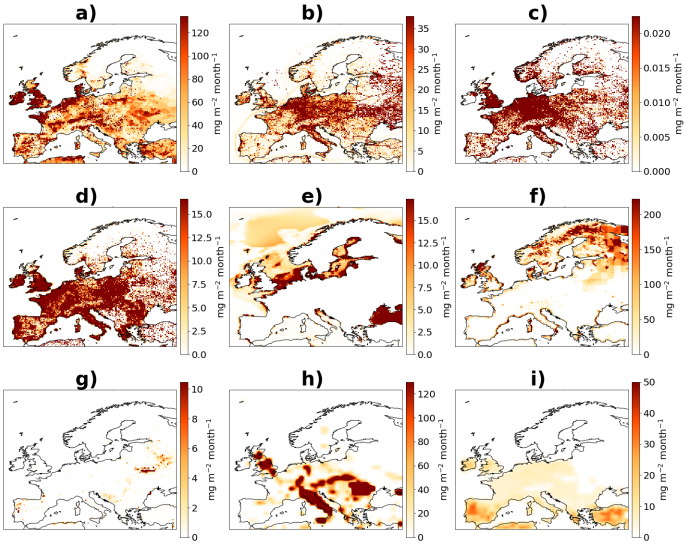

Figure A1. Mean spatial distribution of prior methane (CH_4) fluxes over the inversion domain for 2017–2022. Prior emissions are shown by sector: a) Agriculture (AGR), b) Energy (ENG), c) Industrial processes (IND), d) Waste (WST), e) Ocean (OCE), f) Wetlands and soil sinks (WET), g) Biomass burning (BBR), h) Geological (GEO), and i) Termites (TER). Anthropogenic prior fluxes were derived monthly from GAINS (for EU27+3) and EDGARv8 (for the rest of the world). The GAINS sectors contributing to the AGR, ENG, and WST categories include: Energy: A_PublicPower, B_Industry, D_Fugitives, F_RoadTransport, C_OtherStationaryComb; Agriculture: K_AgriLivestock, L_AgriOther; Waste: J_Waste. The EDGARv8 sectoral inputs correspond to IPCC categories: Energy: BUILDINGS, TRANSPORT, IND_COMBUSTION, POWER_INDUSTRY, FUEL_EXPLOITATION; Industrial processes: IND_PROCESSES; Agriculture; AGRICULTURE; Waste: WASTE.

Table A1: Subregional grouping of European countries used in this study. ISO codes follow ISO 3166-1 alpha-3.

Subregion	Countries
Northern	Denmark (DNK), Estonia (EST), Finland (FIN), Lithuania (LTU), Latvia (LVA), Norway (NOR), Sweden (SWE)
Western	Belgium (BEL), France (FRA), Ireland (IRL), Luxembourg (LUX), Netherlands (NLD), United Kingdom (GBR)
Central	Austria (AUT), Switzerland (CHE), Czech Republic (CZE), Germany (DEU), Hungary (HUN), Poland (POL), Slovakia (SVK)
Southern	Spain (ESP), Italy (ITA), Malta (MLT), Portugal (PRT), Bulgaria (BGR), Cyprus (CYP), Greece (GRC), Croatia (HRV), Romania (ROU), Slovenia (SVN)
BENELUX	Belgium (BEL), Luxembourg (LUX), Netherlands (NLD)
NorCheBri	United Kingdom (GBR), Norway (NOR), Switzerland (CHE)
Scandic	Finland (FIN), Sweden (SWE), Norway (NOR)
EU27+3	Austria (AUT), Belgium (BEL), Bulgaria (BGR), Croatia (HRV), Cyprus (CYP), Czech Republic (CZE), Denmark (DNK), Estonia (EST), Finland (FIN), France (FRA), Germany (DEU), Greece (GRC), Hungary (HUN), Ireland (IRL), Italy (ITA), Latvia (LVA), Lithuania (LTU), Luxembourg (LUX), Malta (MLT), Netherlands (NLD), Poland (POL), Portugal (PRT), Romania (ROU), Slovakia (SVK), Slovenia (SVN), Spain (ESP), Sweden (SWE), United Kingdom (GBR), Norway (NOR), Switzerland (CHE)

https://doi.org/10.5194/egusphere-2025-5877
Preprint. Discussion started: 19 January 2026

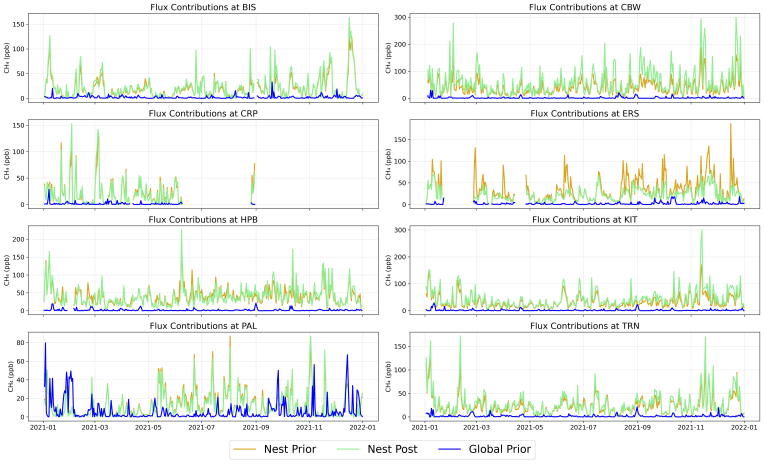

Figure A2. Time series of CH_4 flux contributions from the nested and global domains at selected stations, averaged at the assimilated hour for 2021: BIS (Biscarrosse, France), CBW (Cabauw, Netherlands), CRP (Carnsore Point, Ireland), ERS (Ersa, coastal Mediterranean site), HPB (Hohenpeissenberg, mountain station in Germany), KIT (Karlsruhe, Germany), PAL (Pallas, Finland), and TRN (Trainou, France)

Table A2: List of CH_4 concentration observation sites assimilated in this study. The "Alt" represents the sum of the surface elevation and the intake height above ground level. The "Usage" column uses "M" to denote stations included in the base inversion and "S" to denote stations used only in the sensitivity test. An asterisk (*) in the three-letter station code indicates the station is classified as a mountain station, while a double asterisk (**) indicates the station is classified as a coastal station. Time series of CH_4 concentration are obtained from the ICOS European ObsPack compilation, except for SOD and KMP, which are provided by FMI.

Code	Name/Country	Lat	Lon	Alt	Intake	Usage	Region	PI name / PID
BIK	Bialystok, Poland	53.23	23.01	363	180	M	Central	Christoph Gerbig 11676/dIb_-MKOwY-lXLSoS6Ix_uEH
BIR**	Birkenes, Norway	58.39	8.25	294	75	M	North	Ove Hermansen 11676/Op0FOOTp3OiA0sosQa7c7r8f
BIS**	Biscarrosse, France	44.38	-1.23	120	47	M	Western	Morgan Lopez 11676/CZz7D5w1MOjb5G7tx6OpzF5O
BRM*	Beromunster, Switzerland	47.19	8.18	1009	212	S	Central	Markus Leuenberger 11676/xliOFWs-4Fa8uHRc-f7WdjVt
BSD	Bilsdale, UK	54.36	-1.15	630	248	M	Western	Simon O'Doherty 11676/N_Rk4k74hPRVqQb0LU6dn3MW
CBW	Cabauw, Netherlands	51.97	4.93	207	207	M	Western	Arnoud Frumau 11676/5o7nE4zCWxiOqSOLxy_qPFaa
CMN*	Monte Cimone, Italy	44.19	10.70	2173	8	M	Southern	Paolo Cristofanelli 11676/rV56OWUN0lG6xDvDjAPoUy8P
CRA	Centre Atmosphériques, France	43.13	0.37	630	30	M	Western	Marc Delmotte 11676/B-sdBT0x3-XAOZ1Dv7G0efUO
CRP**	Carnsore Point, Ireland	52.18	-6.37	23	14	M	Western	Damien Martin 11676/3lYhyLy5Op2eKMna-N8MRDeG
ERS**	Ersa, France	42.97	9.38	573	40	M	Southern	Marc Delmotte 11676/eAlLggNtZSSEhLIP4VQF3FzB
FKL	Finokalia, Greece	35.34	25.67	265	15	M	Southern	Marc Delmotte 11676/Z2jyS96qwt8yC9lH0vPKUq9w
GAT	Gartow, Germany	53.07	11.44	411	341	M	Central	Sabrina Arnold 11676/Oc0MscHjLDwjTTROlzNzwecN
HEI	Heidelberg, Germany	49.42	8.68	143	30	S	Central	Samuel Hammer 11676/fSuVm1oug0U-eYnDmY89vvnO
HEL**	Helgoland, Germany	54.18	7.88	153	110	M	Central	Sabrina Arnold 11676/lHon6TrJFT4xSnnWu_t7kiOE
HPB*	Hohenpeissenberg, Germany	47.80	11.03	1065	131	M	Central	Sabrina Arnold 11676/JV5tGrF4G1ki6IuUSSYhud4e
HTM	Hyltemossa, Sweden	56.10	13.42	265	150	M	North	Tobias Biermann 11676/Eve4cRnozSvtdD1uR2J8eQ1e
HUN	Hegyhátsál, Hungary	46.96	16.65	363	115	M	Central	Laszlo Haszpra 11676/nDi91KPtJmGKca15n4OO8K4y
IPR	Ispra, Italy	45.82	8.64	310	100	S	Central	Peter Bergamaschi 11676/6-63kMo0iwyaOG_IDm2e05sI
JFJ	Jungfraujoch, Switzerland	46.55	7.99	3585.7	13.9	S	Central	Lukas Bäni 11676/43dS11kEAb1O1e-CVx4V5FYf

https://doi.org/10.5194/egusphere-2025-5877
Preprint. Discussion started: 19 January 2026

Code	Name/Country	Lat	Lon	Alt	Intake	Usage	Region	PI name / PID
JUE	Jülich, Germany	50.91	6.41	218	120	M	Central	Sabrina Arnold 11676/7-ZcZxJaSr6aYNsPtkxlR5iu
KAS*	Kasprowy Wierch, Poland	49.23	19.98	1994	7	M	Central	Lukasz Chmura 11676/rjzUrVpnGJgkfrE3ivHKM4M4
KIT	Karlsruhe, Germany	49.09	8.43	310	200	M	Central	Sabrina Arnold 11676/xunTpxiKBxeCATiklITfmVfO
KMP**	Kumpula, Finland	60.20	24.96	83	30	M	North	Juha Hatakka
KRE	Křešín u Pacova, Czech Republic	49.57	15.08	784	250	M	Central	Vlastimil Hanuš 11676/OBvoGzvun2yJUhwGSSw_IPFU
LHW	Laegern-Hochwacht, Switzerland	47.48	8.40	872	32	M	Central	Dominik Brunner 11676/ZngGiV560IXmFhPKAvr9VsW9
LIN	Lindenberg, Germany	52.17	14.12	171	98	M	Central	Sabrina Arnold 11676/heVVCRDRi0NAmsTjVT7P5uqx
LMP**	Lampedusa, Italy	35.52	12.63	53	8	M	Southern	Tatiana Di Iorio 11676/iBrGUittGQ0MbSa2d_DRAqSL
LMU	La Muela, Spain	41.60	-1.10	3079	79	M	Southern	Josep-Anton Morguí 11676/RogGl0k9ncLrfQpamPGuHCOw
LUT**	Lutjewad, Netherlands	53.40	6.35	61	60	M	Western	Huilin Chen 11676/-6jCU6FKSHK1QUpTY2ycbA9g
MHD**	Mace Head, Ireland	53.33	-9.90	29	24	M	Western	Morgan Lopez 11676/Z1C0-rDRAwVr_HJqvRWAQ0t-
MLH**	Malin Head, Ireland	55.36	-7.33	69	47	M	Western	Damien Martin 11676/DUzJl8dy-0juDUQpxjkbdZWJ
NOR	Norunda, Sweden	60.09	17.48	146	100	M	North	Irene Lehner 11676/tIU04tuXHJOUQoiUpUx0Lo-m
OHP	Haute, France	43.93	5.71	750	100	M	Western	Pierre-Eric Blanc 11676/eOOPOJiJFIKePdO8pBY3NfWB
OPE	pérenne, France	48.56	5.50	510	120	M	Western	Sébastien Conil 11676/5eJvlDQFaqrMdZJpFeroX0CB
OXK*	Ochsenkopf, Germany	50.03	11.81	1185	163	M	Central	Sabrina Arnold 11676/c-7hY8ADIyUbXnAseeHvPUOG
PAL	Pallas, Finland	67.97	24.12	577	12	M	North	Juha Hatakka 11676/BRQdok2fWTkZjbY2EWt5j_kp
PDM*	Pic du Midi, France	42.94	0.14	2905	28	M	Southern	Marc Delmotte 11676/l78B6eUemNE5fwxPYRmh_aQ5
PRS*	Plateau Rosa, Italy	45.93	7.70	3490	10	M	Southern	Francesco Apadula 11676/EiykeME8LDvWqDMWBnVEl8Dr
PUI	Puijo, Finland	62.91	27.66	316	84	M	North	Kari Lehtinen 11676/oUL5PFu3G24d3faQB8Y32BFX
PUY*	Puy de Dôme, France	45.77	2.97	1475	10	M	Central	Marc Delmotte 11676/Epa5vyYIPOlJgqCvSYf8wKQQ
RGL	Ridge Hill, UK	52.00	-2.54	297	90	M	Western	Simon O'Doherty 11676/uginioEdmGdx6eeXbWCgqqWJ
ROC	Roc'h Trédudon, France	48.41	-3.89	502	140	M	Western	Marc Delmotte 11676/EhkaIxjU0afvi4NoRTPhIjrN
SAC	Saclay, France	48.72	2.14	260	100	M	Western	Marc Delmotte 11676/AoLSAFdhH6ZHK-XKlIWEcMKJ
SMR	Hyytiälä, Finland	61.85	24.30	306	125	M	North	Janne Levula
SOD	Sodankylä, Finland	67.36	26.64	406	179	M	North	Juha Hatakka
SSL*	Schauinsland, Germany	47.92	7.92	1240	35	M	Central	Cédric Couret 11676/-VQ8RK_VTU7EpH65m4nDRt2Z
STE	Steinkimmen, Germany	53.04	8.46	281	252	M	Central	Sabrina Arnold 11676/3aRDFH65i1aOWHtoNhfK0jxp
SVB	Svartberget, Sweden	64.26	19.78	419	150	M	North	Per Marklund 11676/4t7iW7h2mQNwkbokFa5cHn-3
TAC	Tacolneston, UK	52.52	1.14	249	185	M	Western	Simon O'Doherty 11676/pMNbqZiucxfHuFZMSqiec5fB
TOH	Torfhaus, Germany	51.81	10.54	948	147	M	Central	Sabrina Arnold 11676/POM9VeLfoJu7oF5NyCizMoHQ
TRN	Trainou, France	47.97	2.11	311	180	M	Western	Marc Delmotte 11676/IHLvYYV0v68h1XTvHGfACr9D
UTO**	Utö - Baltic Sea, Finland	59.78	21.37	65	57	M	North	Juha Hatakka 11676/4oH7xjDD9SWLlMLmD5vdVHZM
WAO	Weybourne, UK	52.95	1.12	41	10	M	Western	Grant Forster 11676/mf2wNzCd_92k2K4rlbXmA8Xt
WES**	Westerland, Germany	54.92	8.31	26	14	M	Western	Cédric Couret 11676/YO64anbwHvGNYchIXX8dNMsB
ZSF*	Zugspitze, Germany	47.42	10.98	2669	3	M	Central	Cédric Couret 11676/VyAUTyJFxZvM1OPRntBBQr23

Table A3: Prior and posterior model performance statistics at all measurement stations used in this study. The table reports the root-mean-square error (RMSE), mean bias (MBias), and Pearson correlation coefficient (r^2) for both the prior and posterior simulations at the assimilated hour. RMSE and MBias are given in ppb.

Station	RMSE		MBias		r^2	
	Prior	Post	Prior	Post	Prior	Post
bik	24.14	17.68	-11.02	-3.19	0.82	0.88
bir	18.11	14.48	-4.12	2.53	0.77	0.86
bis	25.09	16.66	-11.73	0.47	0.83	0.91

Continued on next page

https://doi.org/10.5194/egusphere-2025-5877
Preprint. Discussion started: 19 January 2026

Station	RMSE		MBias		r^2	
	Prior	Post	Prior	Post	Prior	Post
brm	42.04	26.92	-3.17	-1.62	0.58	0.84
bsd	19.01	16.11	-3.52	-1.38	0.80	0.87
cbw	60.61	35.58	-39.14	-10.21	0.76	0.87
cmn	25.15	19.57	3.87	4.19	0.71	0.80
cra	30.08	18.31	-20.87	-5.42	0.73	0.83
crp	24.80	20.30	-8.00	-3.30	0.83	0.88
ers	24.06	15.33	8.22	1.99	0.79	0.89
fkl	16.10	13.40	4.52	5.54	0.85	0.91
gat	28.05	21.10	-16.75	0.09	0.84	0.87
hel	48.90	30.71	-23.23	-5.64	0.77	0.87
hpb	33.38	26.91	-3.26	4.48	0.66	0.80
htm	23.96	16.17	-11.61	-3.01	0.85	0.92
hun	35.81	26.56	-22.69	-11.52	0.79	0.85
jue	47.85	31.21	-32.05	-6.27	0.78	0.82
kas	24.17	21.52	4.52	10.45	0.74	0.84
kit	35.75	21.43	-21.38	1.09	0.85	0.91
kmp	24.92	17.46	-11.90	-6.11	0.83	0.91
kre	29.25	20.37	-19.33	-4.32	0.83	0.87
lhw	44.04	32.17	-25.31	-12.97	0.70	0.81
lin	34.75	22.26	-22.81	-6.89	0.85	0.90
lmp	20.68	14.00	12.80	7.22	0.83	0.92
lmu	49.36	25.94	-38.78	-9.97	0.51	0.72
lut	94.98	69.98	-48.70	-26.00	0.73	0.82
mhd	16.56	13.81	-2.69	1.31	0.90	0.93
mlh	23.50	19.83	-3.03	-2.28	0.79	0.86
nor	15.21	10.56	-4.75	1.10	0.91	0.95
ope	28.73	17.51	-18.15	-0.79	0.86	0.92
oxk	23.26	17.63	-11.77	1.22	0.75	0.82
pal	14.55	9.78	-5.40	0.56	0.91	0.95
pui	16.15	10.94	-5.14	0.89	0.91	0.95
puy	22.05	15.59	-11.56	1.53	0.83	0.89
rgl	27.74	21.39	-13.88	-7.96	0.84	0.90
roc	28.47	17.80	-15.26	-3.98	0.70	0.86
sac	31.05	21.90	-14.22	0.89	0.87	0.92
smr	14.63	10.34	-4.38	1.37	0.92	0.96
sod	24.17	17.10	-13.57	-6.91	0.84	0.90
ste	55.41	36.62	-37.24	-13.25	0.74	0.82
svb	12.19	9.26	-3.67	1.66	0.94	0.96
toh	22.97	18.42	-13.07	3.42	0.82	0.85
trn	27.80	17.12	-15.49	-1.39	0.85	0.92
uto	18.42	12.42	-4.25	1.13	0.87	0.94
wao	37.63	26.99	-7.12	-1.73	0.77	0.88
wes	57.38	37.85	-27.93	-12.52	0.76	0.87

https://doi.org/10.5194/egusphere-2025-5877
Preprint. Discussion started: 19 January 2026

Table A4: Six-year mean methane fluxes (2017-2022) by region and sector. Values are given in Tg yr^{-1} with ranges in parentheses.

Region/Subregion	Prior Flux	Posterior Flux	Increment (%)
Total Fluxes			
Domain	36.11 (35.54-36.60)	36.70 (35.98-37.38)	+1.62
EU27+3	21.84 (21.13-22.55)	23.28 (22.78-23.85)	+6.56
non EU27+3	14.27 (13.80-14.47)	13.42 (12.98-14.37)	-5.96
EU27	18.80 (18.23-19.33)	20.50 (19.97-21.09)	+9.06
non EU27+3 land	10.26 (9.73-10.49)	9.97 (9.76-10.39)	-2.74
Oceans	5.08 (5.01-5.17)	4.44 (3.89-5.07)	-12.53
Northern	2.07 (2.03-2.18)	2.05 (1.99-2.13)	-1.01
Central	5.19 (4.98-5.53)	6.84 (6.45-7.35)	+31.95
Western	6.36 (6.08-6.65)	7.57 (7.44-7.96)	+19.15
Southern	8.23 (8.04-8.35)	6.81 (6.68-6.98)	-17.25
Benelux	0.92 (0.90-0.96)	1.74 (1.67-1.79)	+88.94
NorCheBri	3.05 (2.90-3.23)	2.78 (2.55-3.04)	-8.83
Scandic	1.50 (1.47-1.61)	1.44 (1.39-1.54)	-4.03
Agricultural Sector			
Domain	11.70 (11.62-11.79)	13.63 (13.42-13.88)	+16.53
EU27+3	8.94 (8.83-9.11)	10.82 (10.61-11.01)	+21.03
non EU27+3	2.76 (2.64-2.82)	2.81 (2.70-2.87)	+1.96
EU27	7.83 (7.73-7.97)	9.67 (9.43-9.81)	+23.48
non EU27+3 land	2.41 (2.29-2.48)	2.45 (2.34-2.50)	+1.57
Oceans	0.76 (0.75-0.77)	0.81 (0.80-0.83)	+6.71
Northern	0.64 (0.63-0.65)	0.68 (0.66-0.69)	+6.59
Central	2.37 (2.35-2.39)	3.19 (3.09-3.31)	+34.63
Western	3.51 (3.45-3.60)	4.54 (4.35-4.72)	+29.26
Southern	2.42 (2.39-2.46)	2.41 (2.37-2.45)	-0.44
Benelux	0.68 (0.67-0.69)	1.29 (1.13-1.38)	+89.87
NorCheBri	1.11 (1.10-1.14)	1.16 (1.11-1.21)	+3.77
Scandic	0.30 (0.30-0.31)	0.31 (0.30-0.31)	+1.99
Energy Sector			
Domain	4.89 (4.57-5.31)	4.71 (4.54-5.03)	-3.71
EU27+3	1.70 (1.58-1.91)	1.77 (1.59-2.03)	+4.18
non EU27+3	3.19 (2.98-3.40)	2.94 (2.82-3.00)	-7.92
EU27	1.53 (1.41-1.74)	1.60 (1.42-1.86)	+4.56
non EU27+3 land	1.81 (1.77-1.85)	1.84 (1.77-1.89)	+1.52
Oceans	1.44 (1.22-1.66)	1.15 (1.04-1.26)	-19.64
Northern	0.07 (0.07-0.07)	0.07 (0.07-0.07)	-0.50
Central	0.81 (0.72-0.95)	0.87 (0.74-1.07)	+8.07
Western	0.31 (0.29-0.33)	0.32 (0.30-0.35)	+3.02
Southern	0.52 (0.49-0.56)	0.51 (0.49-0.55)	-0.59
Benelux	0.06 (0.06-0.06)	0.07 (0.06-0.07)	+8.73
NorCheBri	0.17 (0.17-0.18)	0.17 (0.17-0.18)	+0.75
Scandic	0.04 (0.04-0.05)	0.04 (0.04-0.05)	-0.55
Waste Sector			
Domain	9.60 (9.48-9.74)	9.65 (9.52-9.77)	+0.48
EU27+3	4.90 (4.59-5.32)	4.96 (4.65-5.33)	+1.33
non EU27+3	4.70 (4.41-4.99)	4.68 (4.39-4.97)	-0.40

Continued on next page

https://doi.org/10.5194/egusphere-2025-5877
Preprint. Discussion started: 19 January 2026

Table A4 – continued from previous page

Region/Subregion	Prior Flux	Posterior Flux	Increment (%)
EU27	4.06 (3.87-4.31)	4.13 (3.93-4.37)	+1.70
non EU27+3 land	3.57 (3.33-3.79)	3.56 (3.32-3.78)	-0.20
Oceans	1.39 (1.36-1.45)	1.38 (1.34-1.44)	-0.83
Northern	0.22 (0.21-0.24)	0.23 (0.21-0.24)	+0.50
Central	1.01 (0.92-1.15)	1.05 (0.95-1.20)	+3.84
Western	1.59 (1.43-1.82)	1.64 (1.48-1.82)	+3.20
Southern	2.07 (2.03-2.12)	2.05 (2.01-2.08)	-1.23
Benelux	0.16 (0.14-0.19)	0.18 (0.16-0.21)	+11.02
NorCheBri	0.84 (0.72-1.01)	0.83 (0.72-0.96)	-0.43
Scandic	0.09 (0.09-0.10)	0.09 (0.09-0.10)	-0.25
Wetland Sector			
Domain	2.59 (2.39-2.93)	2.57 (2.42-2.91)	-0.49
EU27+3	1.44 (1.30-1.71)	1.40 (1.30-1.67)	-2.61
non EU27+3	1.14 (1.09-1.26)	1.17 (1.10-1.27)	+2.19
EU27	0.91 (0.78-1.12)	0.89 (0.79-1.11)	-1.66
non EU27+3 land	1.10 (1.05-1.22)	1.13 (1.06-1.23)	+2.36
Oceans	0.09 (0.08-0.10)	0.09 (0.08-0.10)	-2.95
Northern	1.13 (1.10-1.25)	1.10 (1.05-1.22)	-3.27
Central	-0.09 (-0.11–0.04)	-0.08 (-0.10–0.04)	-7.05
Western	0.37 (0.31-0.43)	0.36 (0.30-0.42)	-1.85
Southern	0.03 (-0.07-0.12)	0.03 (-0.07-0.12)	-0.37
Benelux	0.02 (0.01-0.02)	0.02 (0.02-0.02)	+9.53
NorCheBri	0.53 (0.50-0.59)	0.51 (0.48-0.56)	-4.25
Scandic	1.05 (1.00-1.16)	1.01 (0.97-1.13)	-3.62
Geological Sector			
Domain	5.10 (5.10-5.12)	3.47 (3.11-3.77)	-31.98
EU27+3	3.89 (3.89-3.90)	2.51 (2.16-2.76)	-35.42
non EU27+3	1.22 (1.22-1.22)	0.96 (0.87-1.01)	-20.98
EU27	3.56 (3.56-3.56)	2.24 (1.89-2.48)	-37.13
non EU27+3 land	0.63 (0.63-0.63)	0.52 (0.48-0.55)	-16.79
Oceans	0.71 (0.71-0.71)	0.51 (0.41-0.54)	-28.69
Northern	0.02 (0.02-0.02)	0.02 (0.02-0.02)	+0.81
Central	-0.65 (0.65-0.65)	-0.65 (0.56-0.72)	-0.27
Western	0.41 (0.41-0.41)	0.38 (0.34-0.40)	-7.07
Southern	2.81 (2.81-2.82)	1.47 (1.21-1.67)	-47.87
Benelux	0.01 (0.01-0.01)	0.01 (0.01-0.01)	+14.21
NorCheBri	0.33 (0.33-0.33)	0.28 (0.24-0.30)	-17.12
Scandic	0.01 (0.01-0.01)	0.01 (0.01-0.01)	+0.26

Table A5: Comparison of posterior anthropogenic CH_4 emissions (Tg yr^{-1}) for EU27+3 countries with GAINS, UNFCCC, and EDGARv8 inventories, including relative differences (%).

	Emissions (Tg yr^{-1})				Posterior increments (%)		
Country	Posterior	GAINS / Prior	UNFCCC	EDGARv8	Post vs Prior	Post vs UNFCCC	Post vs EDGAR
AUT	0.26	0.22	0.24	0.35	12.74	7.00	-35.06
BEL	0.44	0.27	0.29	0.49	39.75	34.78	-11.26

Continued on next page

https://doi.org/10.5194/egusphere-2025-5877
Preprint. Discussion started: 19 January 2026

Table A5 – continued from previous page

	Emissions (Tg yr^{-1})				Posterior increments (%)		
Country	Posterior	GAINS / Prior	UNFCCC	EDGARv8	Post vs Prior	Post vs UNFCCC	Post vs EDGAR
BGR	0.26	0.26	0.24	0.30	-0.55	7.10	-18.39
CHE	0.17	0.19	0.18	0.20	-13.30	-8.22	-16.22
CYP	0.00	0.00	0.04	0.03	1.00	1.00	1.00
CZE	0.49	0.42	0.49	0.48	13.99	-0.85	1.36
DEU	2.41	1.71	1.75	2.17	29.22	27.38	10.04
DNK	0.26	0.23	0.31	0.29	11.29	-16.00	-7.71
ESP	1.51	1.47	1.49	1.32	2.88	1.66	12.83
EST	0.05	0.05	0.04	0.11	0.52	12.03	-128.64
FIN	0.15	0.15	0.18	0.36	-0.39	-20.28	-140.65
FRA	2.54	2.15	2.30	2.48	15.50	9.52	2.36
GBR	1.89	1.84	1.93	1.68	2.46	-1.99	11.17
GRC	0.35	0.35	0.40	0.26	-1.07	-16.48	24.11
HRV	0.11	0.11	0.15	0.16	2.05	-31.75	-41.13
HUN	0.36	0.35	0.33	0.32	3.42	8.41	11.76
IRL	0.57	0.57	0.62	0.63	-0.11	-8.48	-10.37
ITA	1.51	1.61	1.70	1.23	-6.90	-12.88	18.31
LTU	0.13	0.13	0.12	0.11	2.77	7.28	19.65
LUX	0.03	0.02	0.02	0.03	36.55	27.50	17.78
LVA	0.08	0.08	0.07	0.07	1.48	13.68	16.38
MLT	0.00	0.00	0.01	0.00	1.00	1.00	1.00
NLD	1.07	0.62	0.69	0.62	41.90	35.50	41.54
NOR	0.12	0.12	0.19	0.17	0.28	-64.88	-46.41
POL	1.33	1.22	1.58	1.42	8.06	-19.46	-7.44
PRT	0.44	0.44	0.37	0.26	0.79	15.89	39.93
ROU	0.70	0.70	0.94	0.83	0.24	-34.16	-18.30
SVK	0.13	0.13	0.13	0.16	5.74	0.29	-19.36
SVN	0.10	0.09	0.08	0.08	3.50	21.20	22.56
SWE	0.19	0.18	0.17	0.36	2.76	9.33	-94.28
EU27	17.10	15.11	16.44	16.28	11.66	3.88	4.77
EU27+3	17.64	15.67	17.05	16.96	11.17	3.35	3.89

Code availability. This study makes use of the Community Inversion Framework (CIF) and the Lagrangian transport model FLEXPART, both of which are publicly available. The CIF and FLEXPART codes used for this study are available from the GitLab repositories at https://gitlab.in2p3.fr/satinv/cif and https://gitlab.phaidra.org/flexpart/flexpart/-/releases/v10.4, respectively.

Data availability. The time series of CH_4 dry air mole fraction data used in this study are available from the Integrated Carbon Observation System (ICOS) at https://www.icos-cp.eu/ obspack_CH_4_466_GVeu_v10.0_20240729 European CH_4. Prior emission inventories were obtained from publicly available sources: GAINS (https://iiasa.ac.at/web/home/research/researchPrograms/air/GAINS.html, EDGARv8 (https://edgar.jrc.ec.europa.eu/, and JSBACH-HIMMELI (available upon request from the model developers). Climatological emissions from geological, oceanic, and termite sources follow published datasets cited in this study. Data used for plotting the results of this study will be made available on Zenodo following final publication.

https://doi.org/10.5194/egusphere-2025-5877
Preprint. Discussion started: 19 January 2026

Author contributions. AGM, AT, and TA conceived and designed the study and coordinated the analysis. AGM conducted the inversion runs and prepared the visualisations. AB, AMa, AF and RT developed the CIF-FLEXPART framework and supported model setup. AGM drafted the manuscript with substantial input from AT, HL and TA. AGM, AT, TM, and TA collected and processed the observational and prior data. ALe and MT ran the JSBACH–HIMMELI model and provided the wetland CH_4 emission estimates. LH provided the GAINS CH_4 emissions. ALa contributed methane observations, processing, and analysis. TA and HL provided supervision and resources. All authors contributed to interpreting the results, participated in the scientific discussion, and reviewed and approved the final manuscript.

Competing interests. The authors declare that they have no conflict of interest.

Acknowledgements. We thank the developers and maintainers of the Community Inversion Framework (CIF) and FLEXPART for making their models openly available. We acknowledge the providers of the emission inventories used in this study, including GAINS, EDGARv8, GFED, JSBACH-HIMMELI, and the LPX-Bern DYPTOP v1.4 model for global biospheric emissions. We also thank the European Centre for Medium-Range Weather Forecasts (ECMWF) for providing meteorological data and the Copernicus Atmosphere Monitoring Service (CAMS) for providing background mole fraction data. The authors would like to thank the ICOS and non-ICOS Principal Investigators (PIs) for providing high-quality CH_4 mole-fraction observations (ICOS RI et al., 2023). We acknowledge the PIs and technical teams of the ICOS and non-ICOS stations contributing data to this study (the list of PIs, stations, and PIDs is provided in Appendix A, Table A2). The CH_4 mole fraction data were sourced from the ICOS Carbon Portal: https://doi.org/10.18160/9CQ4-W69K. We thank the Finnish Meteorological Institute for KMP and SOD observations. We also thank colleagues and collaborators for valuable discussions that improved this work, and we are grateful to Tianqi Shi for providing the country mask. We thank the EU-Horizon EYE-CLIMA (101081395) and IM4CA (101183460), the Research Council of Finland projects RCF-GHGSUPER (351311), RCF-CHARM (364975), the RCF Flagships ACCC and FAME (337552 and 359196), WINMET (350184), and FIRI-ICOS Finland (345531), as well as Business Finland BF-AGCLIMATE and the VNK-HIKET for their financial support. We are also grateful to CSC–IT Center for Science, Finland, for providing the high-performance computing resources. We acknowledge the use of AI-assisted tools such as Grammarly and ChatGPT (OpenAI) for improving the language and clarity of the manuscript.

https://doi.org/10.5194/egusphere-2025-5877
Preprint. Discussion started: 19 January 2026

References

Aalto, T., Tsuruta, A., Mäkelä, J., Müller, J., Tenkanen, M., Burke, E., Chadburn, S., Gao, Y., Mannisenaho, V., Kleinen, T., et al.: Air temperature and precipitation constraining the modelled wetland methane emissions in a boreal region in northern Europe, Biogeosciences, 22, 323–340, https://doi.org/10.5194/bg-22-323-2025, 2025.

Bechtold, E. K., Ellenbogen, J. B., Villa, J. A., de Melo Ferreira, D. K., Oliverio, A. M., Kostka, J. E., Rich, V. I., Varner, R. K., Bansal, S., Ward, E. J., et al.: Metabolic interactions underpinning high methane fluxes across terrestrial freshwater wetlands, Nature Communications, 16, 944, https://doi.org/10.1038/s41467-025-56133-0, 2025.

Berchet, A., Sollum, E., Thompson, R. L., Pison, I., Thanwerdas, J., Broquet, G., Chevallier, F., Aalto, T., Bergamaschi, P., Brunner, D., Engelen, R., Fortems-Cheiney, A., Gerbig, C., Groot Zwaaftink, C. D., Haussaire, J.-M., Henne, S., Houweling, S., Karstens, U., Kutsch, W. L., Luijkx, I. T., Monteil, G., Palmer, P. I., van Peet, J. C. A., Peters, W., Peylin, P., Potier, E., Rödenbeck, C., Saunois, M., Scholze, M., Tsuruta, A., and Zhao, Y.: The Community Inversion Framework v1.0: a unified system for atmospheric inversion studies, Geoscientific Model Development, 14, 5331–5354, https://doi.org/10.5194/gmd-14-5331-2021, 2021.

Bergamaschi, P., Corazza, M., Karstens, U., Athanassiadou, M., Thompson, R. L., Pison, I., Manning, A. J., Bousquet, P., Segers, A., Vermeulen, A. T., Janssens-Maenhout, G., Schmidt, M., Ramonet, M., Meinhardt, F., Aalto, T., Haszpra, L., Moncrieff, J., Popa, M. E., Lowry, D., Steinbacher, M., Jordan, A., O'Doherty, S., Piacentino, S., and Dlugokencky, E.: Top-down estimates of European CH4 and N2O emissions based on four different inverse models, Atmospheric Chemistry and Physics, 15, 715–736, https://doi.org/10.5194/acp-15-715-2015, 2015.

Bergamaschi, P., Segers, A., Brunner, D., Haussaire, J.-M., Henne, S., Ramonet, M., Arnold, T., Biermann, T., Chen, H., Conil, S., Delmotte, M., Forster, G., Frumau, A., Kubistin, D., Lan, X., Leuenberger, M., Lindauer, M., Lopez, M., Manca, G., Müller-Williams, J., O'Doherty, S., Scheeren, B., Steinbacher, M., Trisolino, P., Vítková, G., and Yver Kwok, C.: High-resolution inverse modelling of European CH4 emissions using the novel FLEXPART-COSMO TM5 4DVAR inverse modelling system, Atmospheric Chemistry and Physics, 22, 13 243–13 268, https://doi.org/10.5194/acp-22-13243-2022, 2022.

Bergamaschi, P. et al.: Atmospheric CH4 in the first decade of the 21st century: Inverse modeling analysis using SCIAMACHY satellite retrievals and NOAA surface measurements, Journal of Geophysical Research: Atmospheres, 118, 7350–7369, https://doi.org/10.1002/jgrd.50480, 2013.

Bocquet, M. and Sakov, P.: Joint state and parameter estimation with an iterative ensemble Kalman smoother, Nonlinear Processes in Geophysics, 20, 803–818, https://doi.org/10.5194/npg-20-803-2013, 2013.

Cael, B. and Goodwin, P.: Global methane pledge versus carbon dioxide emission reduction, Environmental Research Letters, 18, 104 015, https://doi.org/10.1088/1748-9326/acf8dd, 2023.

Chen, Z., Jacob, D. J., Nesser, H., Sulprizio, M. P., Lorente, A., Varon, D. J., Lu, X., Shen, L., Qu, Z., Penn, E., and Yu, X.: Methane emissions from China: a high-resolution inversion of TROPOMI satellite observations, Atmospheric Chemistry and Physics, 22, 10 809–10 826, https://doi.org/10.5194/acp-22-10809-2022, 2022.

Crippa, M., Solazzo, E., Huang, G., and et al.: High resolution temporal profiles in the Emissions Database for Global Atmospheric Research, Scientific Data, 7, 121, https://doi.org/10.1038/s41597-020-0462-2, 2020.

Dlugokencky, E. J., Nisbet, E. G., Fisher, R., and Lowry, D.: Global atmospheric methane: budget, changes and dangers, Philosophical Transactions of the Royal Society A: Mathematical, Physical and Engineering Sciences, 369, 2058–2072, https://doi.org/10.1098/rsta.2010.0341, 2011.

https://doi.org/10.5194/egusphere-2025-5877
Preprint. Discussion started: 19 January 2026

Ernst, Y., Archibald, S., Balzter, H., Chevallier, F., Ciais, P., Fischer, C. G., and et al.: The African regional greenhouse gases budget (2010–2019), Global Biogeochemical Cycles, 38, e2023GB008 016, https://doi.org/10.1029/2023GB008016, 2024.

Etiope, G., Ciotoli, G., Schwietzke, S., and Schoell, M.: Gridded maps of geological methane emissions and their isotopic signature, Earth System Science Data, 11, 1–22, https://doi.org/10.5194/essd-11-1-2019, 2019.

Friedlingstein, P., O'Sullivan, M., Jones, M. W., Andrew, R. M., Gregor, L., Hauck, J., Le Quéré, C., Luijkx, I. T., Olsen, A., Peters, G. P., Peters, W., Pongratz, J., Schwingshackl, C., Sitch, S., Canadell, J. G., Ciais, P., Jackson, R. B., Alin, S. R., Alkama, R., Arneth, A., Arora, V. K., Bates, N. R., Becker, M., Bellouin, N., Bittig, H. C., Bopp, L., Chevallier, F., Chini, L. P., Cronin, M., Evans, W., Falk, S., Feely, R. A., Gasser, T., Gehlen, M., Gkritzalis, T., Gloege, L., Grassi, G., Gruber, N., Gürses, , Harris, I., Hefner, M., Houghton, R. A., Hurtt, G. C., Iida, Y., Ilyina, T., Jain, A. K., Jersild, A., Kadono, K., Kato, E., Kennedy, D., Klein Goldewijk, K., Knauer, J., Korsbakken, J. I., Landschützer, P., Lefèvre, N., Lindsay, K., Liu, J., Liu, Z., Marland, G., Mayot, N., McGrath, M. J., Metzl, N., Monacci, N. M., Munro, D. R., Nakaoka, S.-I., Niwa, Y., O'Brien, K., Ono, T., Palmer, P. I., Pan, N., Pierrot, D., Pocock, K., Poulter, B., Resplandy, L., Robertson, E., Rödenbeck, C., Rodriguez, C., Rosan, T. M., Schwinger, J., Séférian, R., Shutler, J. D., Skjelvan, I., Steinhoff, T., Sun, Q., Sutton, A. J., Sweeney, C., Takao, S., Tanhua, T., Tans, P. P., Tian, X., Tian, H., Tilbrook, B., Tsujino, H., Tubiello, F., van der Werf, G. R., Walker, A. P., Wanninkhof, R., Whitehead, C., Willstrand Wranne, A., Wright, R., Yuan, W., Yue, C., Yue, X., Zaehle, S., Zeng, J., and Zheng, B.: Global Carbon Budget 2022, Earth System Science Data, 14, 4811–4900, https://doi.org/10.5194/essd-14-4811-2022, 2022.

Gaspari, G. and Cohn, S. E.: Construction of correlation functions in two and three dimensions, Quarterly Journal of the Royal Meteorological Society, 125, 723–757, https://doi.org/10.1002/qj.49712555417, 1999.

Gilbert, J. C. and Lemaréchal, C.: The module M1QN3, Technical report, INRIA Rocquencourt, Domaine de Voluceau, BP 105, 78153 Le Chesnay Cedex, France, available at: file:///home/mengistu/gilbert-lemarechal-2009.pdf, 2009.

Hazan, L., Tarniewicz, J., Ramonet, M., Laurent, O., and Abbaris, A.: Automatic processing of atmospheric CO2 and CH4 mole fractions at the ICOS Atmosphere Thematic Centre, Atmospheric Measurement Techniques, 9, 4719–4736, https://doi.org/10.5194/amt-9-4719-2016, 2016.

Höglund-Isaksson, L., Gómez-Sanabria, A., Klimont, Z., Rafaj, P., and Schöpp, W.: Technical potentials and costs for reducing global anthropogenic methane emissions in the 2050 timeframe – results from the GAINS model, Environmental Research Communications, 2, 025 004, https://doi.org/10.1088/2515-7620/ab7457, 2020.

ICOS RI, Bergamaschi, P., Colomb, A., De Mazière, M., Emmenegger, L., Kubistin, D., Lehner, I., Lehtinen, K., Lund Myhre, C., Marek, M., O'Doherty, S., Platt, S. M., Plaß-Dülmer, C., Ramonet, M., Apadula, F., Arnold, S., Blanc, P.-E., Brunner, D., Chen, H., Chmura, L., Conil, S., Couret, C., Cristofanelli, P., Delmotte, M., Forster, G., Frumau, A., Gheusi, F., Hammer, S., Haszpra, L., Hatakka, J., Heliasz, M., Henne, S., Hoheisel, A., Kneuer, T., Laurila, T., Leskinen, A., Leuenberger, M., Levin, I., Lindauer, M., Lunder, C., Mammarella, I., Manca, G., Manning, A., Martin, D., Meinhardt, F., Mölder, M., Müller-Williams, J., Necki, J., Ottosson-Löfvenius, M., Philippon, C., Piacentino, S., Pitt, J., Rivas-Soriano, P., Scheeren, B., Schumacher, M., Sha, M. K., Smith, P., Spain, G., Steinbacher, M., Sørensen, L. L., Vermeulen, A., Vítková, G., Xueref-Remy, I., di Sarra, A., Conen, F., Kazan, V., Roulet, Y.-A., Biermann, T., Heltai, D., Hensen, A., Hermansen, O., Komínková, K., Laurent, O., Levula, J., Lopez, M., Marklund, P., Pichon, J.-M., Schmidt, M., Stanley, K., Trisolino, P., ICOS Carbon Portal, ICOS Atmosphere Thematic Centre, ICOS Flask And Calibration Laboratory, and ICOS Central Radiocarbon Laboratory: European Obspack compilation of atmospheric methane data from ICOS and non-ICOS European stations for the period 1984-2023; obspack_ch4_466_GVeu_20230913, https://doi.org/10.18160/9CQ4-W69K, 2023.

Ioannidis, E., Meesters, A., Steiner, M., Brunner, D., Reum, F., Pison, I., Berchet, A., Thompson, R., Sollum, E., Koch, F.-T., Gerbig, C., Wang, F., Maksyutov, S., Tsuruta, A., Tenkanen, M., Aalto, T., Monteil, G., Lin, H., Ren, G., Scholze, M., and Houwel-

https://doi.org/10.5194/egusphere-2025-5877
Preprint. Discussion started: 19 January 2026

ing, S.: An inter-comparison of inverse models for estimating European CH_4 emissions, Earth System Science Data Discussions, https://doi.org/10.5194/essd-2025-235, preprint, in review, 2025.

IPCC: 2006 IPCC Guidelines for National Greenhouse Gas Inventories, IPCC Guidelines, https://www.ipcc-nggip.iges.or.jp/public/2006gl/, last access: November 2025, 2006.

IPCC: Refinement to the 2006 IPCC guidelines for national greenhouse gas inventories, IPCC Guidelines for National Greenhouse Gas Inventories., 3, report, https://www.ipcc-nggip.iges.or.jp/public/2019rf/vol5.html(last access: November 2025), 2019.

IPCC: Climate Change 2023: Synthesis Report of the IPCC Sixth Assessment Report (AR6), IPCC Report, https://www.ipcc.ch/report/ar6/syr/, includes statements on global warming potential (GWP) of methane. Last accessed: November 2025, 2023.

IPCC: Climate Change 2021: The Physical Science Basis. Contribution of Working Group I to the Sixth Assessment Report of the Intergovernmental Panel on Climate Change, edited by: Masson-Delmotte, Valérie and Zhai, Panmao and Pirani, Anna and Connors, Sarah L and Péan, Clotilde and Berger, Sophie and Caud, Nada and Chen, Y and Goldfarb, L and Gomis, MI and others, Cambridge University Press, Cambridge, United Kingdom and New York, NY, USA, https://doi.org/10.1017/9781009157896, 2023.

Kikstra, J. S., Nicholls, Z. R. J., Smith, C. J., Lewis, J., Lamboll, R. D., Byers, E., Sandstad, M., Meinshausen, M., Gidden, M. J., Rogelj, J., Kriegler, E., Peters, G. P., Fuglestvedt, J. S., Skeie, R. B., Samset, B. H., Wienpahl, L., van Vuuren, D. P., van der Wijst, K.-I., Al Khourdajie, A., Forster, P. M., Reisinger, A., Schaeffer, R., and Riahi, K.: The IPCC Sixth Assessment Report WGIII climate assessment of mitigation pathways: from emissions to global temperatures, Geoscientific Model Development, 15, 9075–9109, https://doi.org/10.5194/gmd-15-9075-2022, 2022.

Krol, M., Houweling, S., Bregman, B., van den Broek, M., Segers, A., van Velthoven, P., Peters, W., Dentener, F., and Bergamaschi, P.: The two-way nested global chemistry-transport zoom model TM5: algorithm and applications, Atmospheric Chemistry and Physics, 5, 417–432, https://doi.org/10.5194/acp-5-417-2005, 2005.

Leip, A., Skiba, U., Vermeulen, A., and Thompson, R. L.: A complete rethink is needed on how greenhouse gas emissions are quantified for national reporting, Atmospheric Environment, 174, 237–240, https://doi.org/https://doi.org/10.1016/j.atmosenv.2017.12.006, 2018.

Lienert, S. and Joos, F.: A Bayesian ensemble data assimilation to constrain model parameters and land-use carbon emissions, Biogeosciences, 15, 2909–2930, https://doi.org/10.5194/bg-15-2909-2018, 2018.

Monteiro, V. C., Turnbull, J. C., Miles, N. L., Davis, K. J., Barkley, Z., and Deng, A.: Assimilating morning, evening, and nighttime greenhouse gas observations in atmospheric inversions, Journal of Geophysical Research: Atmospheres, 129, e2024JD040 998, https://doi.org/10.1029/2024JD040998, 2024.

Myhre, G., Shindell, D., Bréon, F.-M., Collins, W., Fuglestvedt, J., Huang, J., Koch, D., Lamarque, J.-F., Lee, D., Mendoza, B., Nakajima, T., Robock, A., Stephens, G., Takemura, T., and Zhang, H.: Anthropogenic and Natural Radiative Forcing, in: Climate Change 2013: The Physical Science Basis. Contribution of Working Group I to the Fifth Assessment Report of the Intergovernmental Panel on Climate Change, edited by Stocker, T. F., Qin, D., Plattner, G.-K., Tignor, M., Allen, S. K., Boschung, J., Nauels, A., Xia, Y., Bex, V., and Midgley, P. M., Cambridge University Press, Cambridge, UK and New York, NY, USA, https://www.ipcc.ch/report/ar5/wg1/, chapter in IPCC AR5, 2013.

Peltola, O., Hensen, A., Belelli Marchesini, L., Helfter, C., Bosveld, F. C., van den Bulk, W. C. M., Haapanala, S., van Huissteden, J., Laurila, T., Lindroth, A., Nemitz, E., Röckmann, T., Vermeulen, A. T., and Mammarella, I.: Studying the spatial variability of methane flux with five eddy covariance towers of varying height, Agricultural and Forest Meteorology, 214-215, 456–472, https://doi.org/10.1016/j.agrformet.2015.09.007, 2015.

https://doi.org/10.5194/egusphere-2025-5877
Preprint. Discussion started: 19 January 2026

Peters, W., Miller, J. B., Whitaker, J., Denning, A. S., Hirsch, A., Krol, M. C., Zupanski, D., Bruhwiler, L., and Tans, P. P.: An ensemble data assimilation system to estimate CO_2 surface fluxes from atmospheric trace gas observations, Journal of Geophysical Research: Atmospheres, 110, https://doi.org/10.1029/2005JD006157, 2005.

Petrescu, A. M. R., Qiu, C., Ciais, P., Thompson, R. L., Peylin, P., McGrath, M. J., Solazzo, E., Janssens-Maenhout, G., Tubiello, F. N., Bergamaschi, P., Brunner, D., Peters, G. P., Höglund-Isaksson, L., Regnier, P., Lauerwald, R., Bastviken, D., Tsuruta, A., Winiwarter, W., Patra, P. K., Kuhnert, M., Oreggioni, G. D., Crippa, M., Saunois, M., Perugini, L., Markkanen, T., Aalto, T., Groot Zwaaftink, C. D., Tian, H., Yao, Y., Wilson, C., Conchedda, G., Günther, D., Leip, A., Smith, P., Haussaire, J.-M., Leppänen, A., Manning, A. J., McNorton, J., Brockmann, P., and Dolman, A. J.: The consolidated European synthesis of CH_4 and N_2O emissions for the European Union and United Kingdom: 1990–2017, Earth System Science Data, 13, 2307–2362, https://doi.org/10.5194/essd-13-2307-2021, 2021.

Petrescu, A. M. R., Qiu, C., McGrath, M. J., Peylin, P., Peters, G. P., Ciais, P., Thompson, R. L., Tsuruta, A., Brunner, D., Kuhnert, M., Matthews, B., Palmer, P. I., Tarasova, O., Regnier, P., Lauerwald, R., Bastviken, D., Höglund-Isaksson, L., Winiwarter, W., Etiope, G., Aalto, T., Balsamo, G., Bastrikov, V., Berchet, A., Brockmann, P., Ciotoli, G., Conchedda, G., Crippa, M., Dentener, F., Groot Zwaaftink, C. D., Guizzardi, D., Günther, D., Haussaire, J.-M., Houweling, S., Janssens-Maenhout, G., Kouyate, M., Leip, A., Leppänen, A., Lugato, E., Maisonnier, M., Manning, A. J., Markkanen, T., McNorton, J., Muntean, M., Oreggioni, G. D., Patra, P. K., Perugini, L., Pison, I., Raivonen, M. T., Saunois, M., Segers, A. J., Smith, P., Solazzo, E., Tian, H., Tubiello, F. N., Vesala, T., van der Werf, G. R., Wilson, C., and Zaehle, S.: The consolidated European synthesis of CH_4 and N_2O emissions for the European Union and United Kingdom: 1990–2019, Earth System Science Data, 15, 1197–1268, https://doi.org/10.5194/essd-15-1197-2023, 2023.

Pisso, I., Sollum, E., Grythe, H., Kristiansen, N. I., Cassiani, M., Eckhardt, S., Arnold, D., Morton, D., Thompson, R. L., Groot Zwaaftink, C. D., Evangeliou, N., Sodemann, H., Haimberger, L., Henne, S., Brunner, D., Burkhart, J. F., Fouilloux, A., Brioude, J., Philipp, A., Seibert, P., and Stohl, A.: The Lagrangian particle dispersion model FLEXPART version 10.4, Geoscientific Model Development, 12, 4955–4997, https://doi.org/10.5194/gmd-12-4955-2019, 2019.

Qu, Z., Jacob, D. J., Shen, L., Lu, X., Zhang, Y., Scarpelli, T. R., Nesser, H., Sulprizio, M. P., Maasakkers, J. D., Bloom, A. A., Worden, J. R., Parker, R. J., and Delgado, A. L.: Global distribution of methane emissions: a comparative inverse analysis of observations from the TROPOMI and GOSAT satellite instruments, Atmospheric Chemistry and Physics, 21, 14 159–14 175, https://doi.org/10.5194/acp-21-14159-2021, 2021.

Raivonen, M., Smolander, S., Backman, L., Susiluoto, J., Aalto, T., Markkanen, T., Mäkelä, J., Rinne, J., Peltola, O., Aurela, M., Lohila, A., Tomasic, M., Li, X., Larmola, T., Juutinen, S., Tuittila, E.-S., Heimann, M., Sevanto, S., Kleinen, T., Brovkin, V., and Vesala, T.: HIMMELI v1.0: HelsinkI Model of MEthane buiLd-up and emIssion for peatlands, Geoscientific Model Development, 10, 4665–4691, https://doi.org/10.5194/gmd-10-4665-2017, 2017.

Ramonet, M., Ciais, P., Apadula, F., Bartyzel, J., Bastos, A., Bergamaschi, P., and Yver Kwok, C.: The fingerprint of the summer 2018 drought in Europe on ground-based atmospheric CO_2 measurements, Philosophical Transactions of the Royal Society B: Biological Sciences, 375, https://doi.org/10.1098/rstb.2019.0513, 2020.

Rayner, T. and Jordan, A.: Climate Change Policy in the European Union, https://doi.org/10.1093/acrefore/9780190228620.013.47, 2016.

Reick, C. H., Gayler, V., Goll, D., Hagemann, S., Heidkamp, M., Nabel, J. E. M. S., and et al.: JSBACH 3 - The land component of the MPI Earth System Model: documentation of version 3.2, Tech. Rep. 240, Berichte zur Erdsystemforschung, https://doi.org/10.17617/2.3279802, 2021.

Saunois, M., Stavert, A. R., Poulter, B., Bousquet, P., Canadell, J. G., Jackson, R. B., Raymond, P. A., Dlugokencky, E. J., Houweling, S., Patra, P. K., Ciais, P., Arora, V. K., Bastviken, D., Bergamaschi, P., Blake, D. R., Brailsford, G., Bruhwiler, L., Carlson, K. M., Carrol,

https://doi.org/10.5194/egusphere-2025-5877
Preprint. Discussion started: 19 January 2026

M., Castaldi, S., Chandra, N., Crevoisier, C., Crill, P. M., Covey, K., Curry, C. L., Etiope, G., Frankenberg, C., Gedney, N., Hegglin, M. I., Höglund-Isaksson, L., Hugelius, G., Ishizawa, M., Ito, A., Janssens-Maenhout, G., Jensen, K. M., Joos, F., Kleinen, T., Krummel, P. B., Langenfelds, R. L., Laruelle, G. G., Liu, L., Machida, T., Maksyutov, S., McDonald, K. C., McNorton, J., Miller, P. A., Melton, J. R., Morino, I., Müller, J., Murguia-Flores, F., Naik, V., Niwa, Y., Noce, S., O'Doherty, S., Parker, R. J., Peng, C., Peng, S., Peters, G. P., Prigent, C., Prinn, R., Ramonet, M., Regnier, P., Riley, W. J., Rosentreter, J. A., Segers, A., Simpson, I. J., Shi, H., Smith, S. J., Steele, L. P., Thornton, B. F., Tian, H., Tohjima, Y., Tubiello, F. N., Tsuruta, A., Viovy, N., Voulgarakis, A., Weber, T. S., van Weele, M., van der Werf, G. R., Weiss, R. F., Worthy, D., Wunch, D., Yin, Y., Yoshida, Y., Zhang, W., Zhang, Z., Zhao, Y., Zheng, B., Zhu, Q., Zhu, Q., and Zhuang, Q.: The Global Methane Budget 2000–2017, Earth System Science Data, 12, 1561–1623, https://doi.org/10.5194/essd-12-1561-2020, 2020.

Saunois, M., Martinez, A., Poulter, B., Zhang, Z., Raymond, P. A., Regnier, P., Canadell, J. G., Jackson, R. B., Patra, P. K., Bousquet, P., Ciais, P., Dlugokencky, E. J., Lan, X., Allen, G. H., Bastviken, D., Beerling, D. J., Belikov, D. A., Blake, D. R., Castaldi, S., Crippa, M., Deemer, B. R., Dennison, F., Etiope, G., Gedney, N., Höglund-Isaksson, L., Holgerson, M. A., Hopcroft, P. O., Hugelius, G., Ito, A., Jain, A. K., Janardanan, R., Johnson, M. S., Kleinen, T., Krummel, P. B., Lauerwald, R., Li, T., Liu, X., McDonald, K. C., Melton, J. R., Mühle, J., Müller, J., Murguia-Flores, F., Niwa, Y., Noce, S., Pan, S., Parker, R. J., Peng, C., Ramonet, M., Riley, W. J., Rocher-Ros, G., Rosentreter, J. A., Sasakawa, M., Segers, A., Smith, S. J., Stanley, E. H., Thanwerdas, J., Tian, H., Tsuruta, A., Tubiello, F. N., Weber, T. S., van der Werf, G. R., Worthy, D. E. J., Xi, Y., Yoshida, Y., Zhang, W., Zheng, B., Zhu, Q., Zhu, Q., and Zhuang, Q.: Global Methane Budget 2000–2020, Earth System Science Data, 17, 1873–1958, https://doi.org/10.5194/essd-17-1873-2025, 2025.

Seibert, P. and Frank, A.: Source-receptor matrix calculation with a Lagrangian particle dispersion model in backward mode, Atmospheric Chemistry and Physics, 4, 51–63, https://doi.org/10.5194/acp-4-51-2004, 2004.

Shen, L., Jacob, D. J., Gautam, R., Omara, M., Scarpelli, T. R., Lorente, A., Zavala-Araiza, D., Lu, X., Chen, Z., and Lin, J.: National quantifications of methane emissions from fuel exploitation using high resolution inversions of satellite observations, Nature Communications, 14, 4948, https://doi.org/10.1038/s41467-023-40671-6, 2023.

Solazzo, E., Crippa, M., Guizzardi, D., Muntean, M., Choulga, M., and Janssens-Maenhout, G.: Uncertainties in the Emissions Database for Global Atmospheric Research (EDGAR) emission inventory of greenhouse gases, Atmospheric Chemistry and Physics, 21, 5655–5683, https://doi.org/10.5194/acp-21-5655-2021, 2021.

Steiner, M., Peters, W., Luijkx, I., Henne, S., Chen, H., Hammer, S., and Brunner, D.: European CH_4 inversions with ICON-ART coupled to the CarbonTracker Data Assimilation Shell, Atmospheric Chemistry and Physics, 24, 2759–2782, https://doi.org/10.5194/acp-24-2759-2024, 2024.

Stohl, A., Wotawa, G., Seibert, P., and Kromp-Kolb, H.: Interpolation errors in wind fields as a function of spatial and temporal resolution and their impact on different types of kinematic trajectories, Journal of Applied Meteorology and Climatology, 34, 2149–2165, https://doi.org/10.1175/1520-0450(1995)034<2149:IEIWFA>2.0.CO;2, 1995.

Szénási, B., Berchet, A., Broquet, G., Segers, A., van der Gon, H. D., Krol, M., Hullegie, J. J., Kiesow, A., Günther, D., Petrescu, A. M. R., Saunois, M., Bousquet, P., and Pison, I.: A pragmatic protocol for characterising errors in atmospheric inversions of methane emissions over Europe, Tellus B: Chemical and Physical Meteorology, 73, 1–23, https://doi.org/10.1080/16000889.2021.1914989, 2021.

Tenkanen, M. K., Tsuruta, A., Denier van der Gon, H., Höglund-Isaksson, L., Leppänen, A., Markkanen, T., Petrescu, A. M. R., Raivonen, M., Aaltonen, H., and Aalto, T.: Partitioning anthropogenic and natural methane emissions in Finland during 2000–2021 by combining bottom-up and top-down estimates, Atmospheric Chemistry and Physics, 25, 2181–2206, https://doi.org/10.5194/acp-25-2181-2025, 2025.

https://doi.org/10.5194/egusphere-2025-5877
Preprint. Discussion started: 19 January 2026

Thompson, R. L. and Stohl, A.: FLEXINVERT: an atmospheric Bayesian inversion framework for determining surface fluxes of trace species using an optimized grid, Geoscientific Model Development, 7, 2223–2242, https://doi.org/10.5194/gmd-7-2223-2014, 2014.

Tipka, A., Haimberger, L., and Seibert, P.: Flex_extract v7.1.2 – a software package to retrieve and prepare ECMWF data for use in FLEXPART, Geoscientific Model Development, 13, 5277–5310, https://doi.org/10.5194/gmd-13-5277-2020, 2020.

Tsuruta, A., Aalto, T., Backman, L., Krol, M. C., Peters, W., Lienert, S., and Gomez-Pelaez, A. J.: Methane budget estimates in Finland from the CarbonTracker Europe-CH4 data assimilation system, Tellus B: Chemical and Physical Meteorology, 71, 1565 030, https://doi.org/10.1080/16000889.2018.1565030, 2019.

Tsuruta, A., Kivimäki, E., Lindqvist, H., Karppinen, T., Backman, L., Hakkarainen, J., Schneising, O., Buchwitz, M., Lan, X., Kivi, R., Chen, H., Buschmann, M., Herkommer, B., Notholt, J., Roehl, C., Té, Y., Wunch, D., Tamminen, J., and Aalto, T.: CH4 Fluxes Derived from Assimilation of TROPOMI XCH4 in CarbonTracker Europe-CH4: Evaluation of Seasonality and Spatial Distribution in the Northern High Latitudes, Remote Sensing, 15, 1620, https://doi.org/10.3390/rs15061620, 2023.

van der Werf, G. R., Randerson, J. T., Giglio, L., van Leeuwen, T. T., Chen, Y., Rogers, B. M., Mu, M., van Marle, M. J. E., Morton, D. C., Collatz, G. J., Yokelson, R. J., and Kasibhatla, P. S.: Global fire emissions estimates during 1997–2016, Earth System Science Data, 9, 697–720, https://doi.org/10.5194/essd-9-697-2017, 2017.

Vermeulen, A. T., Hensen, A., Popa, M. E., van den Bulk, W. C. M., and Jongejan, P. A. C.: Greenhouse gas observations from Cabauw Tall Tower (1992–2010), Atmospheric Measurement Techniques, 4, 617–644, https://doi.org/10.5194/amt-4-617-2011, 2011.

Villani, M. G., Bergamaschi, P., Krol, M., Meirink, J. F., and Dentener, F.: Inverse modeling of European CH4 emissions: sensitivity to the observational network, Atmospheric Chemistry and Physics, 10, 1249–1267, https://doi.org/10.5194/acp-10-1249-2010, 2010.

Voigt, C., Virkkala, A. M., Hould Gosselin, G., et al.: Arctic soil methane sink increases with drier conditions and higher ecosystem respiration, Nature Climate Change, 13, 1095–1104, https://doi.org/10.1038/s41558-023-01785-3, 2023.

Weber, T., Wiseman, N. A., and Kock, A.: Global ocean methane emissions dominated by shallow coastal waters, Nature Communications, 10, 4584, https://doi.org/10.1038/s41467-019-12541-7, 2019.

WMO: Greenhouse Gas concentrations hit record high. Again., https://wmo.int/news/media-centre/greenhouse-gas-concentrations-hit-record-high-again, last accessed: November 2025, 2023.